

NATIONAL ADVISORY COMMITTEE FOR AERONAUTICS

TECHNICAL NOTE 2584

AN ANALYSIS OF FLOW IN ROTATING PASSAGE OF LARGE
RADIAL-INLET CENTRIFUGAL COMPRESSOR AT
TIP SPEED OF 700 FEET PER SECOND

By Vasily D. Prian and Donald J. Michel

Lewis Flight Propulsion Laboratory
Cleveland, Ohio



Washington

December 1951

AFMDC
TECHNICAL LIBRARY
AEL 2811

319.98/41



1L

NATIONAL ADVISORY COMMITTEE FOR AERONAUTICS

TECHNICAL NOTE 2584

AN ANALYSIS OF FLOW IN ROTATING PASSAGE OF LARGE

RADIAL-INLET CENTRIFUGAL COMPRESSOR AT

TIP SPEED OF 700 FEET PER SECOND

By Vasily D. Prian and Donald J. Michel

SUMMARY

An analysis was made of the flow in the rotating passages of a 48-inch diameter radial-inlet centrifugal impeller at a tip speed of 700 feet per second in order to provide more knowledge on the flow conditions within the impeller.

This analysis indicated that the region of low efficiency generally existed along the trailing face as a result of a combination of shifting of low energy air toward the trailing face and losses arising from the decelerations along the trailing face.

Because of comparatively large viscous losses along the trailing face, and with unloading of the blades, the velocity at the driving face tip was higher than at the trailing face tip. This velocity difference would be expected to result in mixing losses upon diffusion of the air. The experimental and theoretical distributions of torque on the blades were approximately the same. The theoretically predicted eddy on the driving face was not found experimentally. The modification of the theoretical entrance angle of flow for the first 15 percent of the passage gave fair agreement between the theoretical and experimental static pressures at off-design conditions except for the maximum flow conditions.

INTRODUCTION

Analyses of centrifugal-compressor performance have been limited by lack of knowledge of detailed flow conditions within the rotating passage and by lack of rapid theoretical methods of analysis. Some rigorous theoretical methods of compressor analysis have been developed for two-dimensional, nonviscous, compressible flow for specific blade shapes (references 1 and 2). However, the general use of these methods has

PERMANENT
RECORD

not been found feasible because of the extremely tedious and laborious manual calculating techniques involved in the application of the methods to blades of arbitrary shape. Recently, several rapid theoretical methods of analysis have been proposed and investigated. One of these, a simplified theory for two-dimensional, nonviscous, compressible flow, was developed in reference 3.

Successful experimental determination of flow conditions within the rotating passages of a 48-inch radial impeller operating at a low tip speed has been accomplished recently at the NACA Lewis laboratory and is reported in reference 4. The rapid method of analysis developed in reference 3 has been applied to this impeller at weight flows for which experimental data are available and the results of the analysis are presented herein.

Because of the complicated viscous effects associated with compressors which cannot yet be predicted theoretically, exact agreement between theoretical and experimental flow cannot be expected. However, trends predicted by the theoretical analysis are expected to show up in the experimental data. A comparison of these trends and a study of the variation in flow condition due to viscous effects are presented in an attempt to provide more knowledge on flow conditions within the rotating impeller passage.

APPARATUS AND PROCEDURE

The impeller and compressor over-all instrumentation used in the experimental investigation are described in reference 4. Table I gives the pertinent blade data for the impeller. The blade thickness was corrected to account for the difference in blade area above and below the mean height. Hence the actual passage area at any radius may be computed from the blade height and corrected thickness without consideration of blade taper (fig. 3(b)). The impeller installation is shown in figure 1. In addition to the previously described instruments (reference 4), the total pressure and temperature were measured in the diffuser at $1\frac{1}{2}$ impeller radius position near the diffuser tip in three peripheral positions. Four probe calibrated rakes were used to measure the pressure and temperature.

The instrument locations are shown in figure 2. The static and total pressure probes used for determining the experimental velocities along the blade surfaces are located on geometric streamlines 1 and 9 rather than on the blades. The instruments and the pressure transfer device are fully described in reference 4.

The operating procedure was the same as that reported in reference 4.

COMPUTATIONAL PROCEDURES

The rapid approximate method of determining velocities on impeller blades developed in reference 3 was adapted and modified to apply to the 48-inch radial-inlet centrifugal impeller without changing the basic assumptions of the method.

The equations for determining the velocities on the blade surfaces are developed in reference 3. The equations used herein for the blade surface velocities are:

$$Q_d = Q_{av} - \frac{\frac{d}{dR} (Q_{av} \sin \beta R \Delta \theta) + 2M_T R \Delta \theta}{\frac{2}{\cos \beta}} \quad (1)$$

$$Q_t = 2Q_{av} - Q_d \quad (2)$$

(All symbols are defined in appendix A.) Equation (1) results directly from the equation (16) of reference 3 for a constant-thickness radial-flow blade. The velocity Q_{av} is based on the continuity and energy considerations and can be calculated by the simultaneous solution of the following equations (modified from reference 3):

$$Q_{av} = \frac{\frac{1}{\rho_0 c_0} \frac{\Delta w}{(\Delta a)_T}}{\frac{\rho_{av}}{\rho_0} \cos \beta_{av} HR \frac{\Delta \theta}{(\Delta \theta)_T}} \quad (3)$$

$$\frac{\rho_{av}}{\rho_0} = \left\{ 1 + \frac{\gamma-1}{2} \left[(RM_T)^2 - Q_{av}^2 \right] \right\}^{\frac{1}{\gamma-1}} \quad (4)$$

in which Δw is the incremental flow rate through the passage between two blades and $(\Delta a)_T$ is the incremental flow area (between the two blades) normal to the velocity Q_{av} at the impeller tip.

In equation (1) the term $RA\theta$ represents the net passage area, taking into account the large fillet on the trailing face of the blade. The blade angles of both the driving and trailing faces were approximately equal except for a small portion of the entrance section (fig. 3(a)) so the driving-face blade angle was used in equation (1). The velocity profile was altered near the tip to take into account the slip factor by the method presented in reference 3. The slip factor used in the computations was that experimentally determined for each weight flow considered and for this impeller became effective gradually starting at $R = 0.7821$.

The theoretical static pressure was determined by use of equation (24) of reference 3:

$$\frac{p}{p_0} = \left\{ 1 + \frac{\gamma-1}{2} \left[(RM_T)^2 - Q^2 \right] \right\}^{\frac{\gamma}{\gamma-1}} \quad (5)$$

the last term $(-2M_T\lambda_U)$ in equation (24) is dropped out since $\lambda_U = 0$ (λ_U is whirl ratio).

The theoretical isentropic total pressure was determined from the expression:

$$\frac{P}{P_0} = \left[1 + \left(\frac{\gamma-1}{2} \right) M_T^2 R^2 \right]^{\frac{\gamma}{\gamma-1}} \quad (6)$$

The expression for the relative adiabatic efficiency η_{ad}

$$\eta_{ad} = \frac{2gJc_p T_0 \left[\left(\frac{P_r}{P_0} \right)^{\frac{\gamma-1}{\gamma}} - 1 \right]}{\omega^2 r^2} \quad (7)$$

is developed in reference 4.

The experimental velocities were obtained by using the expression:

$$q = \frac{\omega^2 r^2 + 2gJc_p T_0}{1 + \frac{1}{\left[\left(\frac{P}{p} \right)^{\frac{\gamma-1}{\gamma}} - 1 \right]}} \quad (8)$$

The velocity ratio Q is then computed as the ratio of the computed velocity to the absolute stagnation speed of sound upstream of the impeller entrance. The complete development of equation (8) is given in appendix B.

In the expression (8) for velocity at any point within the impeller, the velocity is primarily dependent on the ratio $\left(\frac{P}{p}\right)^{\frac{\gamma-1}{\gamma}}$. Thus, a small error in the value of P or p gives a large error in the value of q when the ratio P/p is small. For example, when the value of Q is of the order of 0.10, an error of ± 0.5 percent (experimental error) in both total and static pressures gives an error in velocity ratio of approximately 50 percent. However, at $Q = 0.50$, the same pressure error gives a velocity error of only 3 percent. For this reason, the velocities in the low range can be considered only qualitatively and only the trends can be considered.

For each weight flow condition, the average angle of attack at the inlet was computed from the experimental relative velocity at the center of the passage between the blades. This angle of attack was then faired in with the geometric blade angle over the first 15 percent of the passage in applying the simplified analysis method of reference 3.

Comparison of the experimental angle of attack of zero with a theoretical angle of attack based on isentropic flow conditions indicated that a correction for the inlet area should be made. The area of the blade is subtracted from the area of the annulus in computing the angle of attack at the blade inlet. At angles of attack other than zero, the experimentally observed angle of attack was approximately one-half the theoretical value after the area correction was made.

The angle of attack is considered to be zero when the flow angle of the air is equal to the blade angle β as shown in figure 3(a). For a flow angle of the air greater than the blade angle the angle of attack is positive. Conversely, for a flow angle of the air less than the blade angle the angle of attack is negative.

RESULTS AND DISCUSSION

Impeller and Diffuser Performance

The variation of the adiabatic efficiency η_{ad} at the diffuser exit with the corrected weight flow $\frac{W\sqrt{\theta}}{\delta}$ is shown in figure 4. The efficiency of 0.80, which occurred at a weight flow of 26.25 pounds per

second, appears to be the peak. This peak-efficiency weight flow corresponded closely to the weight flow at which the computed angle of attack on the blade driving face was zero. This weight flow condition is referred to as the "design condition" throughout this report.

The efficiency drops off on either side of the peak, and the conditions at the extremes are referred to as "off-design conditions". In this report the weight flow of 14 pounds per second, which is near surge, is discussed as the flow condition at a large positive angle of attack while weight flows of 44 and 32 pounds per second are discussed as flow conditions for negative angles of attack.

Design Flow Characteristics

The experimental total-pressure distribution (measured along geometric streamlines 1 and 9, fig. 2) from inlet to tip along the blade surfaces (fig. 5(a)) indicates that the total pressure along the driving face is practically equal to the theoretical value for isentropic flow (within experimental error), whereas, along the trailing face the total pressure is lower than the isentropic value for most of the passage length, especially close to the blade tip. Theoretically, for nonviscous flow the total pressure would be constant across the passage at any given radius. The drop in the experimental total pressure across the passage from driving to trailing face is further illustrated in figure 5(b). The pressure near the trailing face (geometric streamline 9) between $R = 20$ and 22.5 inches is slightly higher than the pressure nearer the passage center. This rise causes the trailing face pressure, as illustrated in figure 5(a), to be nearer the isentropic value at the 20-inch radius. The variation of the experimental pressure from the theoretical isentropic value is shown in figure 5(c) by means of constant pressure-loss contours throughout the passage. The greatest losses in the passage occur near the trailing face tip. For about half of the passage width on the driving face side, there are no losses. The losses at the entrance to the blades are slight. The relative adiabatic efficiency contours are shown in figure 5(d). Because there were no losses near the driving face, the efficiency remained 1.0 for most of the passage length. A drop in efficiency across the passage toward the trailing blade tip to about 0.80 is observed. Figure 5(c) and equation (7) indicate that, if no further losses occur as energy is added to the fluid as it moves radially outward, the relative efficiency will increase. However, the apparent increase in efficiency from 0.95 to 1.0 (fig. 5(d)) at the entrance is not possible for the two-dimensional case and presumably results from a secondary flow in the hub-shroud plane.

A comparison of the theoretically predicted static-pressure distribution along the blade surfaces and the experimentally determined

static-pressure distribution is shown in figure 5(e). Good agreement exists over most of the passage except for the entrance and tip. The experimental and theoretical pressure differences across the blade over the blade length are approximately the same, indicating that distributions of the ideal and experimental torque are approximately the same. The trends of the slopes of both the driving and trailing faces indicate that the static pressures are equal at the impeller tip, indicating the necessary unloading of the blade at the tip.

The experimental static-pressure distribution across the passage at varying radii (fig. 5(f)) generally agrees well with the theoretical patterns found in references 1 and 2, with a large slope from the driving to the trailing face in the passage center, and lesser slopes at the entrance and tip. The velocity distributions along the blade faces and throughout the passage, plotted as constant velocity ratio contours, are presented in figures 5(g) and 5(h), respectively. Figure 5(g) shows a decelerating velocity along the trailing face from the 14-inch radius to the impeller outlet. This deceleration is not desirable from the standpoint of boundary-layer build-up and possibly exceeds the maximum gradient at which separation may be avoided. At present experimental data are insufficient to determine whether separation exists. However, if separation does not exist, this gradient results in an undesirable thick region of low-energy air (boundary layer) that results in losses along the trailing face. At the 14-inch radius the relative efficiency decreases (fig. 5(d)) and this decrease continues to the outlet.

Near the entrance along the driving face there is a large deceleration with no loss in efficiency. It is believed that because of the pressure gradient from the driving face to the trailing face the boundary layer is removed by a secondary flow and by bleeding of the boundary layer through the clearance space between the blade and the shroud.

The shifting of low-energy air toward the trailing face is possibly a major cause of the loss in relative efficiency along the trailing face and causes other losses.

In figure 5(g), the eddy which was theoretically predicted along the driving face (the negative velocity between $r = 18$ in. and $r = 20$ in.) was not found in the experimental investigation. Even though the possible error in the quantitative value of the velocity ratio is large, the experimental results give no indication of reverse flow, which would be expected in an eddy. The reduction in effective flow area due to viscous effects and the increase in specific volume are probably the reasons for the absence of the eddy.

The unloading of the blade at the tip and the drop in total pressure from the driving to the trailing face due to the losses incurred in the passage result in a velocity difference across the blade at the exit. The velocity at the driving face tip is higher than that at the

trailing face tip, as shown in figures 5(g) and 5(h). This is contrary to the theoretical studies, which show the velocity to be equal for the isentropic flow where the blade unloads. This velocity difference across the blade results in mixing losses upon diffusion of the air. Consequently, poor impeller design results in poor diffuser performance.

Off-Design Flow Characteristics

Positive angle of attack. - The flow characteristics in the impeller rotating passage at a weight flow of 14 pounds per second are shown in figure 6. The trends of the total-pressure distribution (figs. 6(a) and 6(b)) are similar to those for design conditions (figs. 5(a) and 5(b)). As at design flow, the total pressure appears to be higher than isentropic, because of the experimental error. However, there is a larger loss of total pressure along the trailing face, and some change in pressure-loss configuration (figs. 5(c) and 6(c)). The relative efficiency contours (fig. 6(d)) indicate a low efficiency region about halfway through the impeller at the trailing face and a relative rise in efficiency from there to the impeller outlet. A comparison of the theoretical and experimental static-pressure distributions along the blade surfaces (fig. 6(e)) shows fair agreement over most of the passage. For the entrance section of the passage a flow-angle correction was made according to the method described in the computing procedure. The static-pressure distribution across the passages (fig. 6(f)) shows the same trends as those at design flow.

The experimental velocity distributions along the blade faces (fig. 6(g)) did not agree with the theoretical distributions and the large eddy predicted theoretically did not occur. The velocity decelerated from the 13-inch radius to about the 20-inch radius over which distance the relative efficiency constantly decreased (figs. 6(h) and 6(d)).

Negative angle of attack. - The flow characteristics in the impeller rotating passage at the choked flow condition (44 lb/sec) are shown in figure 7. The large negative angle of attack caused a severe drop in total pressure from the theoretical isentropic value along the driving face entrance (fig. 7(a)). The pressure builds up again, probably by some secondary flow process in the hub-shroud plane, but never reaches the isentropic value as it did at the lower weight-flow conditions. The experimental data indicated a reversed flow at the driving face entrance. Along the trailing face, the total pressure remains approximately equal to the isentropic value for about half the passage length and then drops off toward the tip. The high pressure-loss region tends to move outward and across the passage towards the trailing face to the middle of the stream (fig. 7(b)). The total-pressure distribution curves give an indication of the losses in the passage. As at

design flow, the greatest loss (other than that due to entrance conditions) occurs at the trailing face tip.

The static-pressure distributions along the blade faces and across the passage (figs. 7(c) and 7(d)) have the same complex trends as the total pressures, caused by the entrance conditions.

There is some agreement in trend between the experimental and the theoretical relative velocities along the blade surfaces (fig. 7(e)) from the 16-inch radius to the impeller outlet. However, magnitudes of the theoretical values are appreciably lower than the experimental values. The entrance velocity from the 12-inch radius to the 16-inch radius at the driving face could not be measured because of the reversed flow.

In order to show trends of flow at a slight negative angle of attack, the flow characteristics in the impeller rotating passage at a corrected weight flow of 32 pounds per second are presented in figure 8. The flow tends to follow the same trends as design flow after about 15 percent of the passage is passed. The initial irregularities are caused by the entrance angle of the air. The total-pressure loss at this driving face entrance indicates possible separation around the sharp edge of the blade at a negative angle of attack.

SUMMARY OF RESULTS

From an analysis of the flow in the rotating passage of the 48-inch radial-inlet centrifugal impeller the following results were obtained:

1. A region of low efficiency generally existed along the trailing face. This low energy region probably arose through a combination of a shifting of low energy air toward the trailing face and losses resulting from the decelerations along the same face.
2. Because of comparatively large viscous losses along the trailing face, and with unloading of the blade, the velocity at the trailing face tip was of necessity lower than that at the driving face. This velocity difference would be expected to result in mixing losses upon diffusion of the air.
3. The experimental static-pressure difference across the blades was approximately the same as the theoretical static-pressure difference, indicating the same distribution of torque on the blade.
4. The modification of the theoretical entrance angle of flow for the first 15 percent of the passage gave fair agreement between the

theoretical and experimental static pressures at design and off-design conditions except for the maximum flow condition.

5. The theoretically predicted eddy on the driving face was not found in the experimental investigation.

Lewis Flight Propulsion Laboratory
National Advisory Committee for Aeronautics
Cleveland, Ohio, August 23, 1951

APPENDIX A

SYMBOLS

The following symbols are used in this report:

c_0	stagnation speed of sound upstream of impeller
c_p	specific heat of air at constant pressure, ft-lb/(lb)(°F)
g	acceleration due to gravity, ft/sec ²
H	ratio of impeller blade height to impeller tip blade height
J	mechanical equivalent of heat, ft-lb/Btu
M_T	impeller tip Mach number
P	total pressure, in. Hg
ΔP	total-pressure loss, in. Hg
p	static pressure, in. Hg
Q	ratio of relative velocity to stagnation speed of sound upstream of impeller
q	stream velocity, ft/sec
R	ratio of impeller radius to impeller tip radius
r	impeller radius, ft
T	total temperature, °R
t	static temperature, °R
W	air weight flow, lb/sec
β	blade angle (fig. 3(a))
γ	ratio of specific heats
δ	ratio of actual inlet total pressure to standard sea-level pressure, 29.92 in. Hg
η_{ad}	adiabatic efficiency

θ ratio of actual inlet total temperature to standard sea-level temperature, 518.4° R

$\Delta\theta$ angular width of passage between blades

ρ density

ω rotor speed, radians/sec

Subscripts:

av average

d driving face of blade

r relative

T impeller tip

t trailing face of blade

O upstream measuring station

APPENDIX B

CALCULATION OF EXPERIMENTAL VELOCITY

IN IMPELLER PASSAGE

The expression for the experimental velocity in the impeller passage is derived in the following manner:

$$c_p t_r + \frac{q^2}{2gJ} = c_p T_0 + \frac{\omega^2 r^2}{2gJ} = c_p T_r \quad (1)$$

$$2gJc_p t_r = \omega^2 r^2 - q^2 + 2gJc_p T_0 \quad (1a)$$

Since

$$c_p t_r = c_p T_r - \frac{q^2}{2gJ} \quad (2)$$

$$c_p (t_r - T_r) = - \frac{q^2}{2gJ} \quad (2a)$$

$$c_p t_r \left(1 - \frac{T_r}{t_r} \right) = - \frac{q^2}{2gJ} \quad (2b)$$

But

$$\frac{T_r}{t_r} = \left(\frac{P_r}{P_r} \right)^{\frac{\gamma-1}{\gamma}} \quad (3)$$

Substitution of equation (3) in equation (2b) gives

$$c_p t_r \left[1 - \left(\frac{P_r}{P_r} \right)^{\frac{\gamma-1}{\gamma}} \right] = - \frac{q^2}{2gJ}$$

or

$$2gJc_p t_r = - \frac{q^2}{\left[1 - \left(\frac{P_r}{P_r} \right)^{\frac{\gamma-1}{\gamma}} \right]} \quad (4)$$

When equation (1a) and equation (4) are equated,

$$\frac{-q^2}{\left[1 - \left(\frac{P_r}{P_r} \right)^{\frac{\gamma-1}{\gamma}} \right]} = \omega^2 r^2 - q^2 + 2gJc_p T_0 \quad (5)$$

$$q^2 - \frac{q^2}{\left[1 - \left(\frac{P_r}{P_r} \right)^{\frac{\gamma-1}{\gamma}} \right]} = \omega^2 r^2 + 2gJc_p T_0 \quad (5a)$$

$$q^2 \left\{ 1 - \frac{1}{\left[1 - \left(\frac{P_r}{P_r} \right)^{\frac{\gamma-1}{\gamma}} \right]} \right\} = \omega^2 r^2 + 2gJc_p T_0 \quad (5b)$$

$$q^2 = \frac{\omega^2 r^2 + 2gJc_p T_0}{1 - \frac{1}{\left[1 - \left(\frac{P_r}{P_r} \right)^{\frac{\gamma-1}{\gamma}} \right]}} \quad (5c)$$

or rearrangement of the last term yields

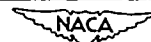
$$q = \sqrt{\frac{\omega^2 r^2 + 2gJc_p T_0}{1 + \frac{1}{\left[\left(\frac{P_r}{P_r} \right)^{\frac{\gamma-1}{\gamma}} - 1 \right]}}}$$

REFERENCES

1. Stanitz, John D., and Ellis, Gaylord O.: Two-Dimensional Compressible Flow in Centrifugal Compressors with Straight Blades. NACA Rep. 954, 1950. (Formerly NACA TN 1932.)
2. Ellis, Gaylord O., and Stanitz, John D.: Two-Dimensional Compressible Flow in Centrifugal Compressors with Logarithmic-Spiral Blades. NACA TN 2255, 1951.
3. Stanitz, John D., and Prian, Vasily D.: A Rapid Approximate Method for Determining Velocity Distribution on Impeller Blades of Centrifugal Compressors. NACA TN 2421, 1951.
4. Michel, Donald J., Ginsburg, Ambrose, and Mizisin, John: Experimental Investigation of Flow in the Rotating Passages of a 48-inch Impeller at Low Tip Speeds. NACA RM E51D20, 1951.

TABLE I - BLADE DATA AT MEAN HEIGHT¹

Radius (in.)	Blade angle (deg)	Total blade height (in.)	Thickness (in.)	
			Actual	Corrected
12.3	57.7	3.30	0.730	0.897
13.0	55.3	3.05	.714	.873
14.0	50.9	2.72	.665	.817
16.0	37.3	2.23	.531	.654
18.0	20.0	1.91	.445	.545
20.0	4.0	1.69	.410	.504
21.5	0	1.53	.397	.487
22.5	0	1.45	.389	.478
23.5	4.4	1.40	.380	.467

¹Data taken from reference 4.

2376



Figure 1. - Radial-inlet impeller used in experimental investigation of flow within rotating passages.

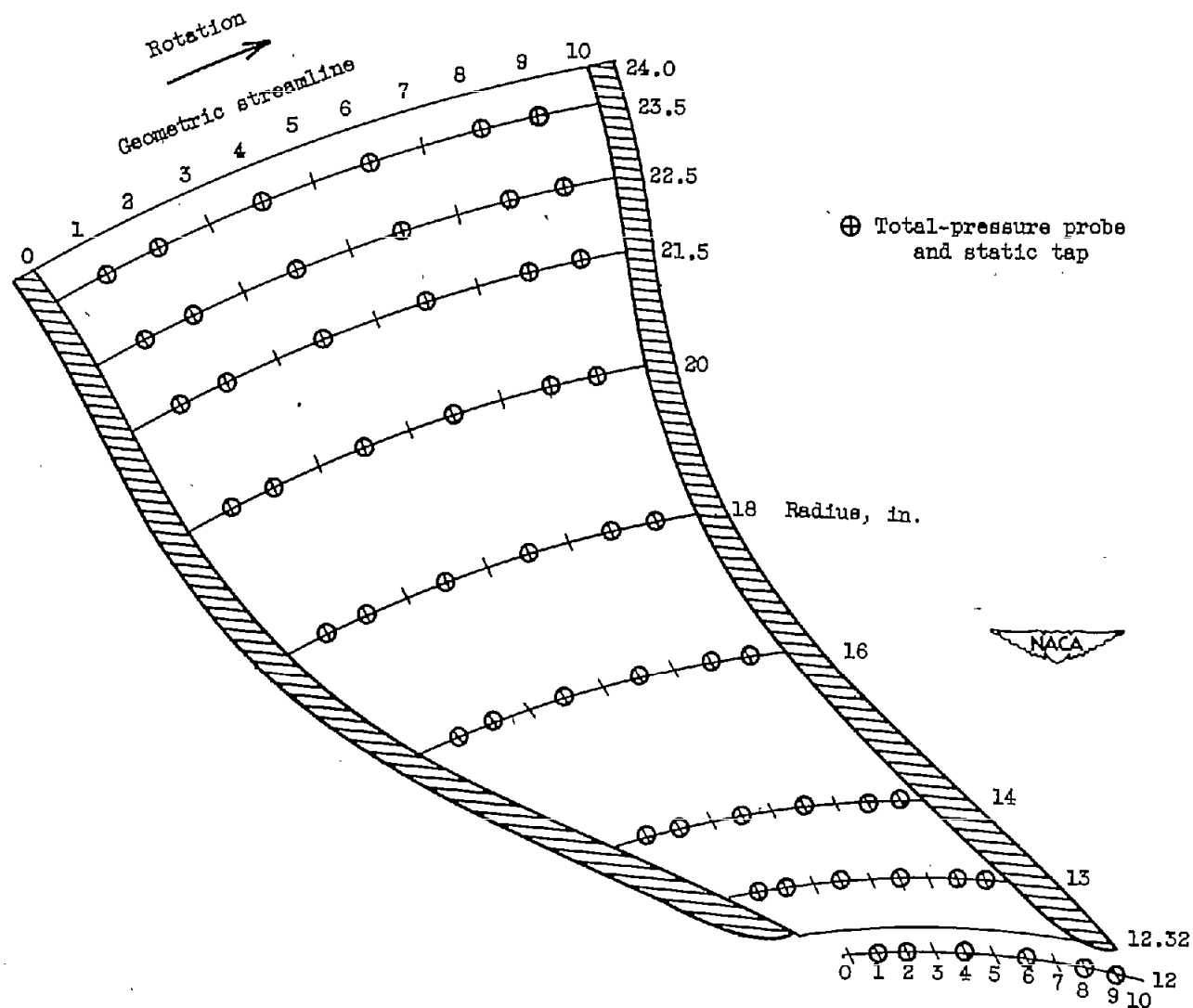
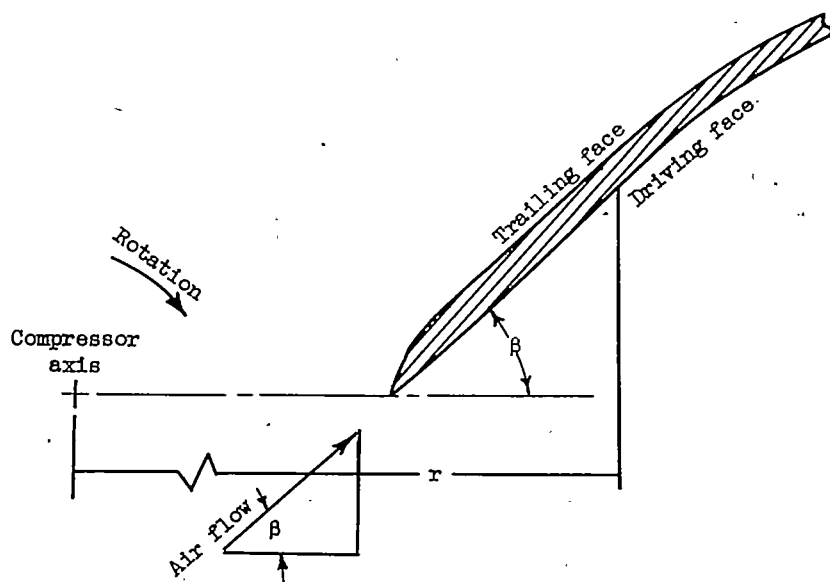
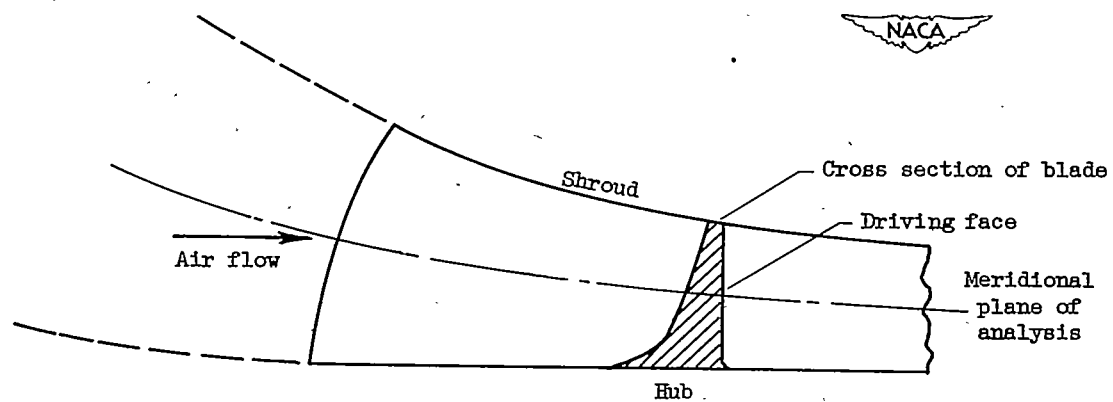


Figure 2. - Instrument locations in rotating impeller passage.

2376



(a) Cross section of blade along meridional plane.



(b) Side view of blade.

Figure 3. - Sketch of impeller blade.

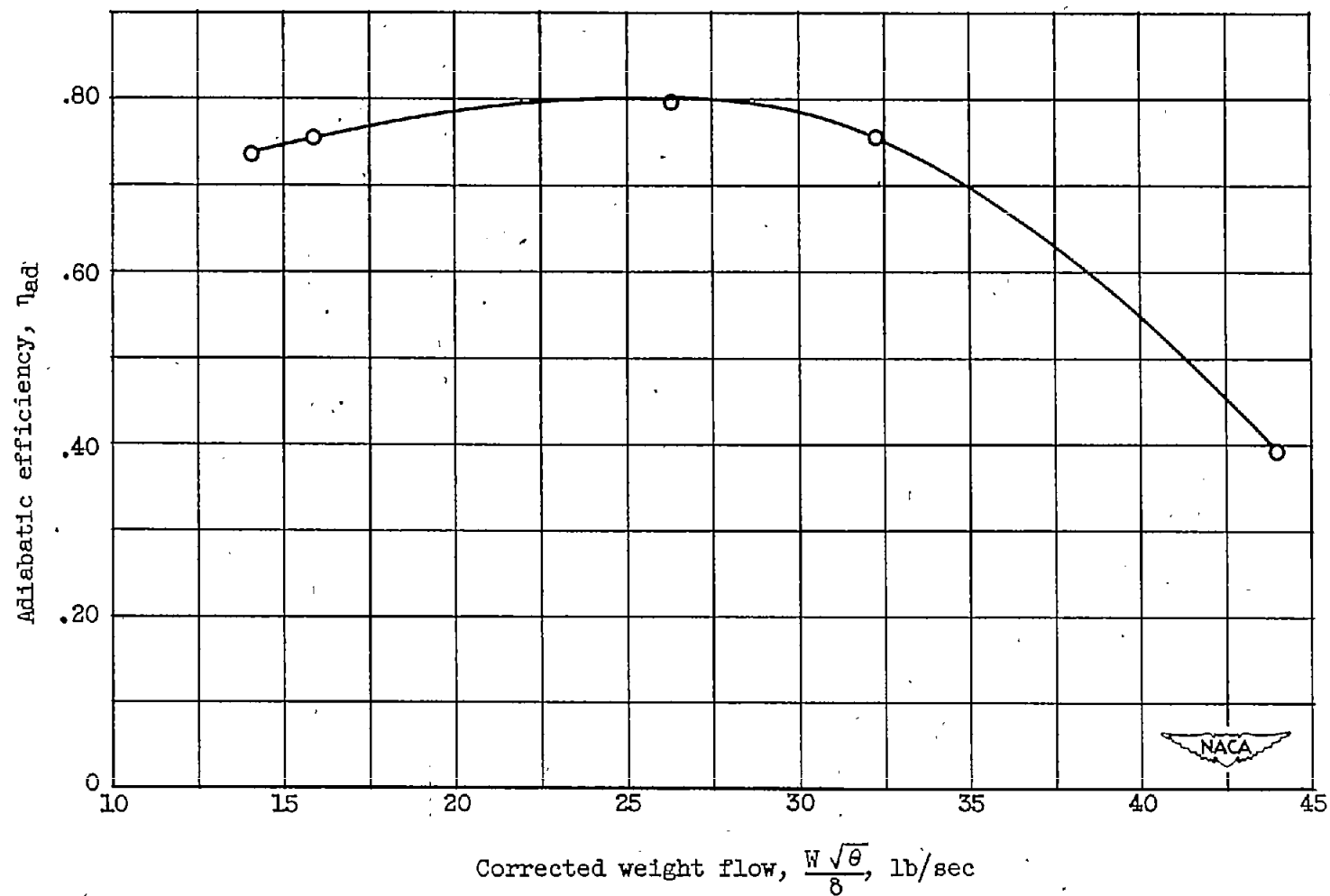
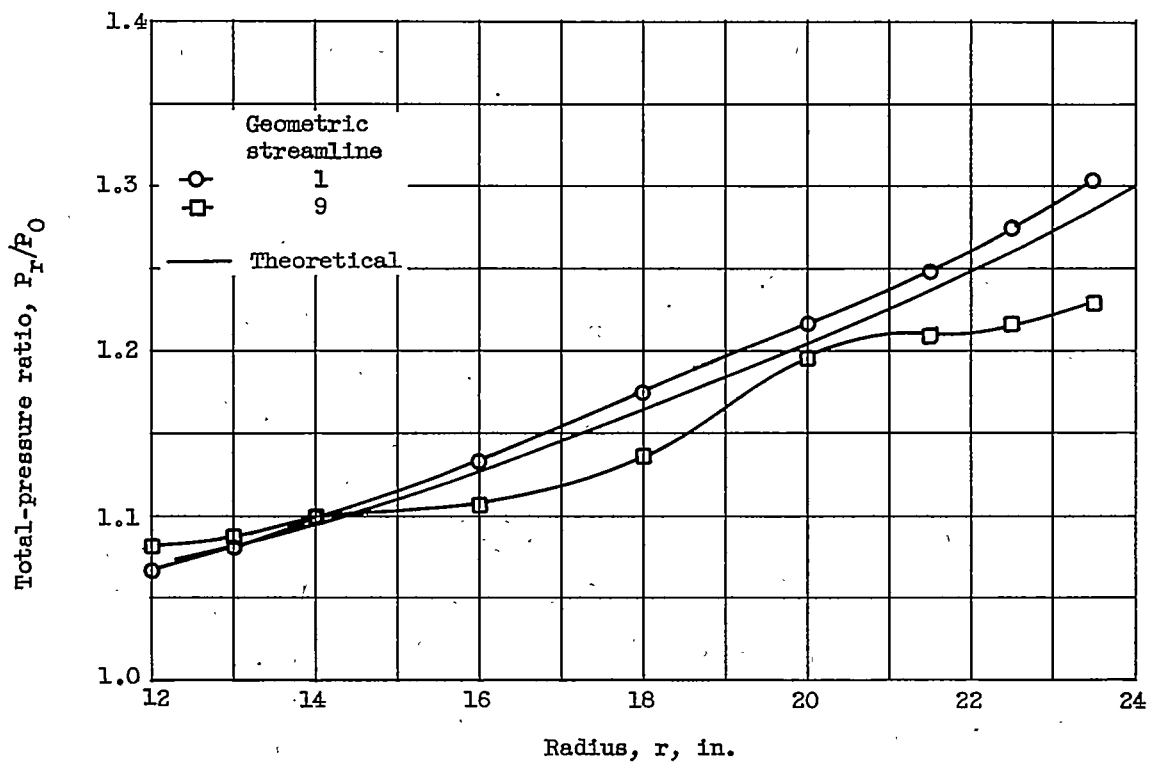
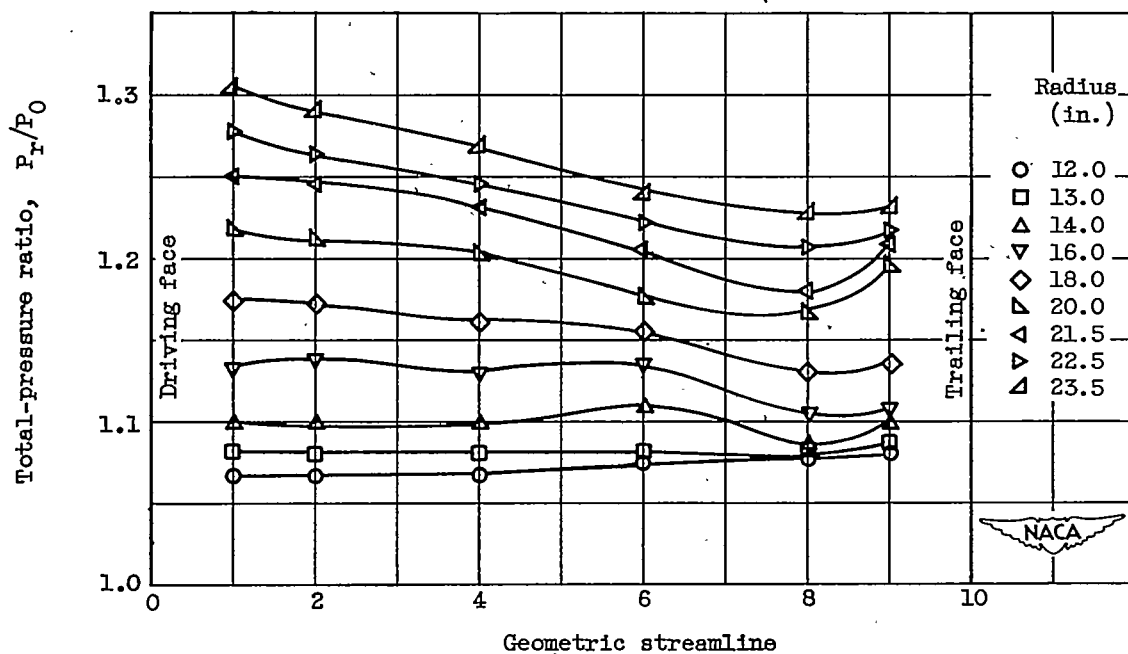


Figure 4. - Adiabatic efficiency of impeller and vaneless diffuser based on conditions at diffuser tip ($1\frac{1}{2}$ impeller radii).

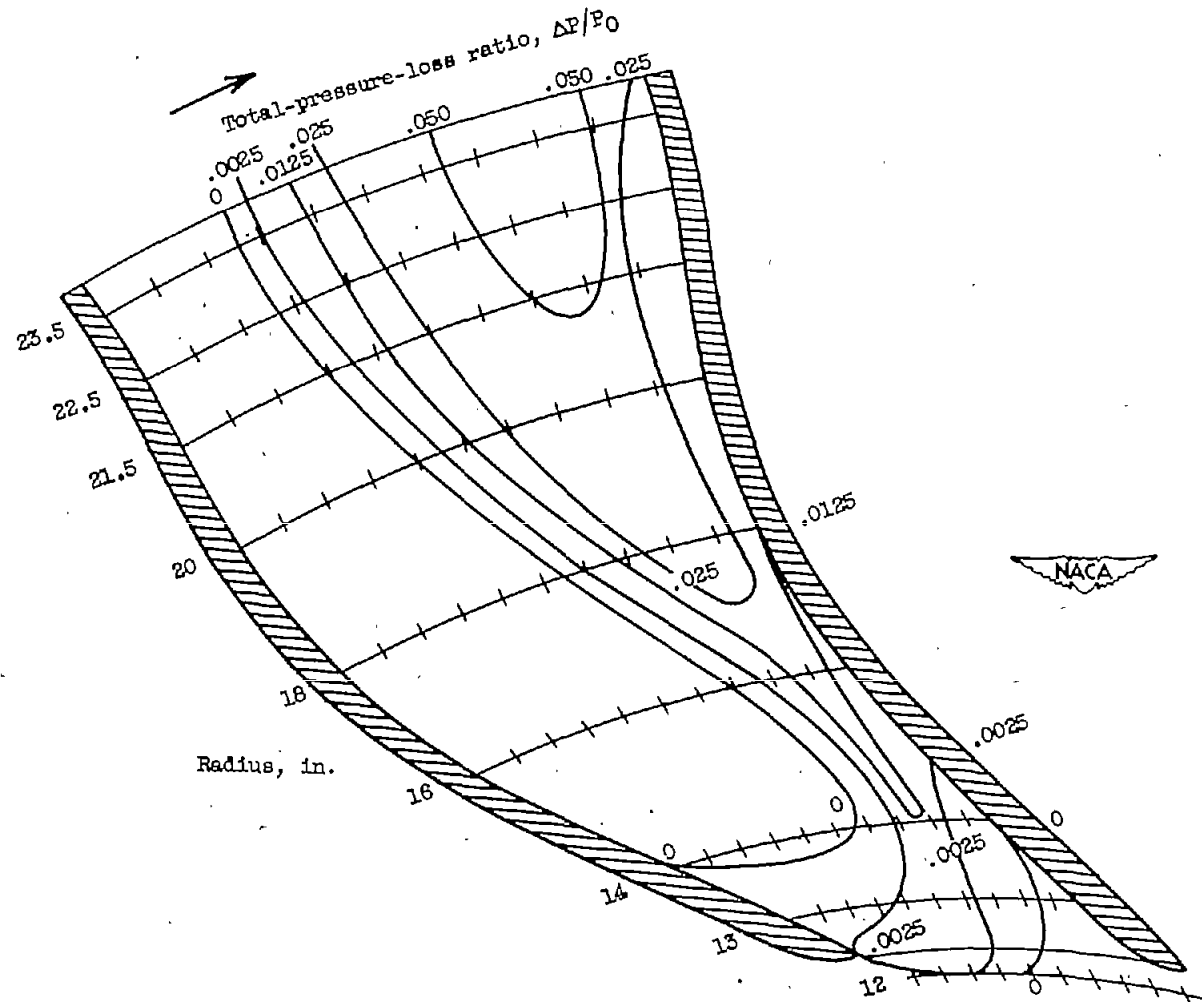


(a) Total-pressure distribution along blade faces.



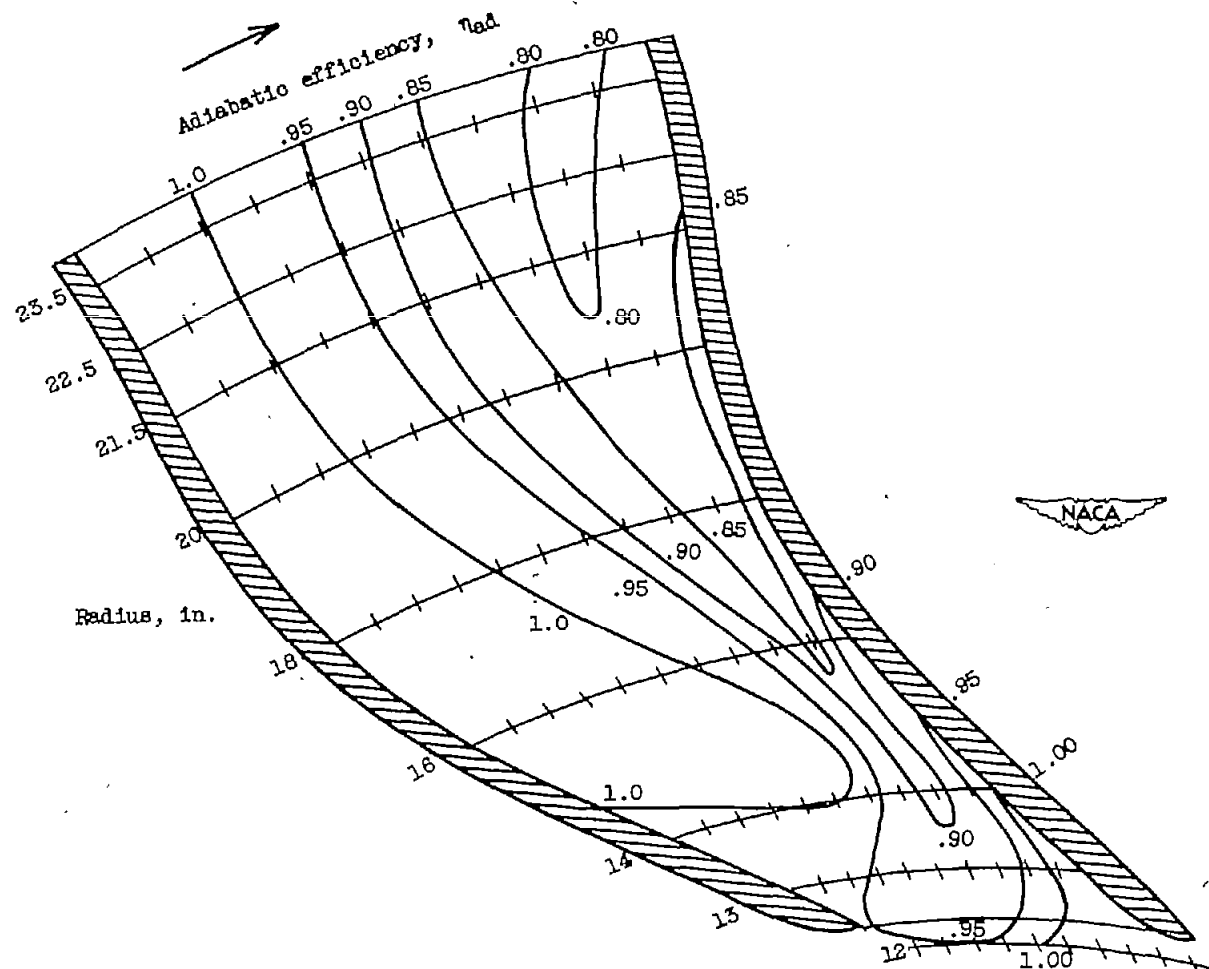
(b) Total-pressure distribution across passage.

Figure 5. - Flow characteristics in impeller rotating passage at corrected weight flow of 26 pounds per second.



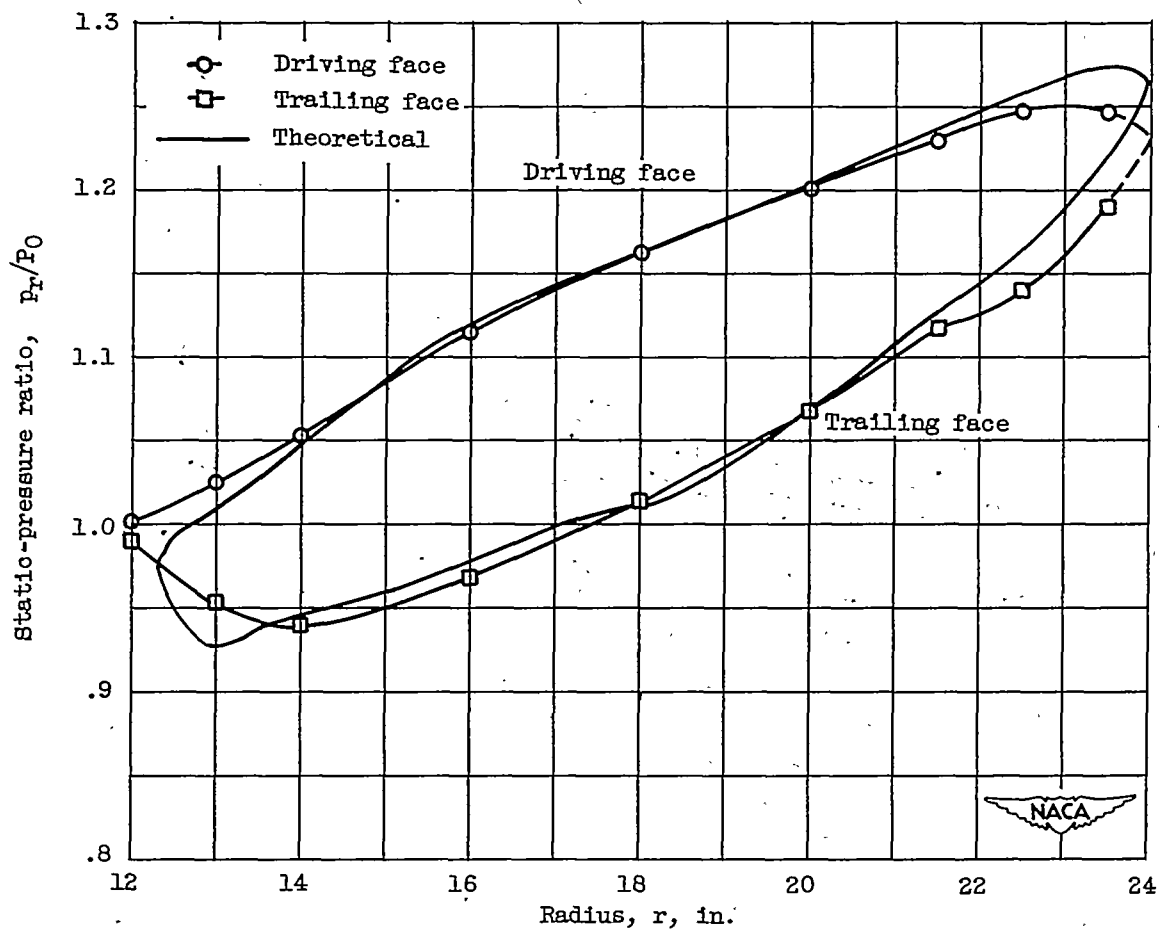
(c) Total-pressure-loss distribution throughout passage.

Figure 5. - Continued. Flow characteristics in impeller rotating passage at corrected weight flow of 26 pounds per second.



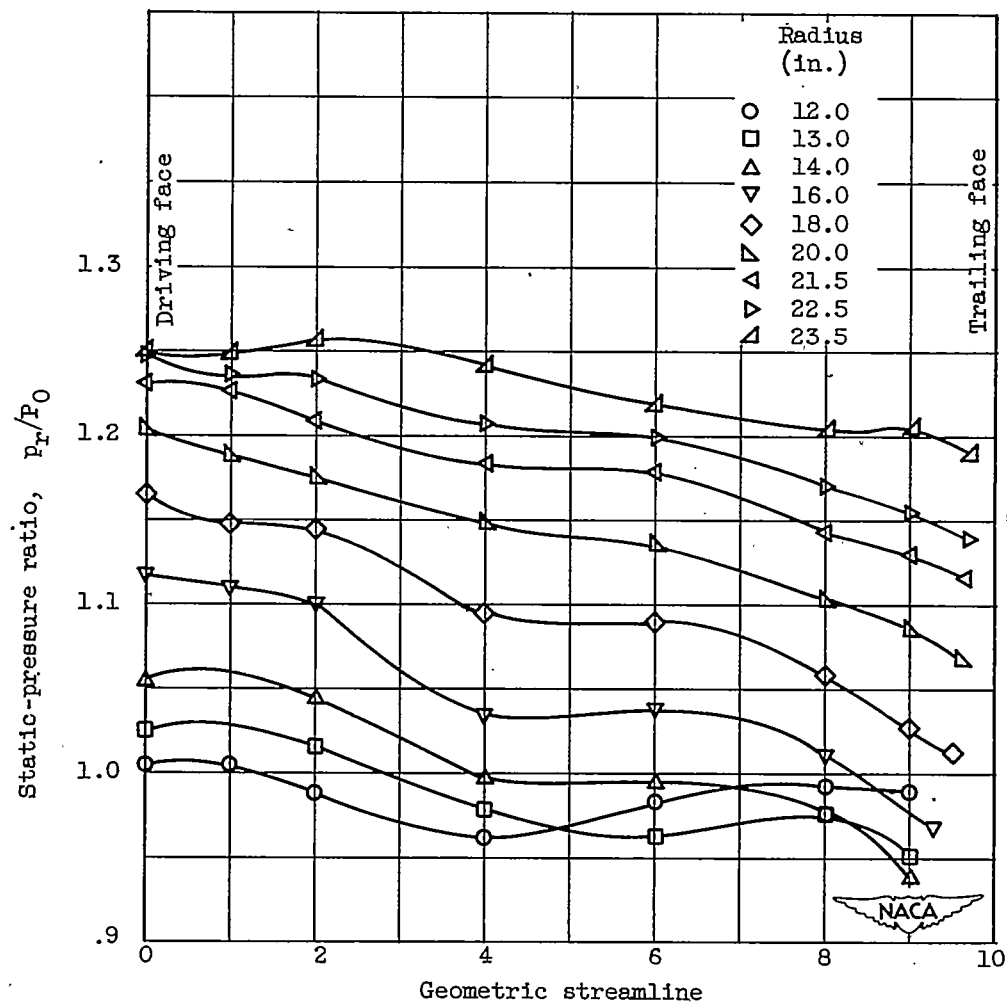
(d) Efficiency distribution throughout passage.

Figure 5. - Continued. Flow characteristics in impeller rotating passage at corrected weight flow of 26 pounds per second.



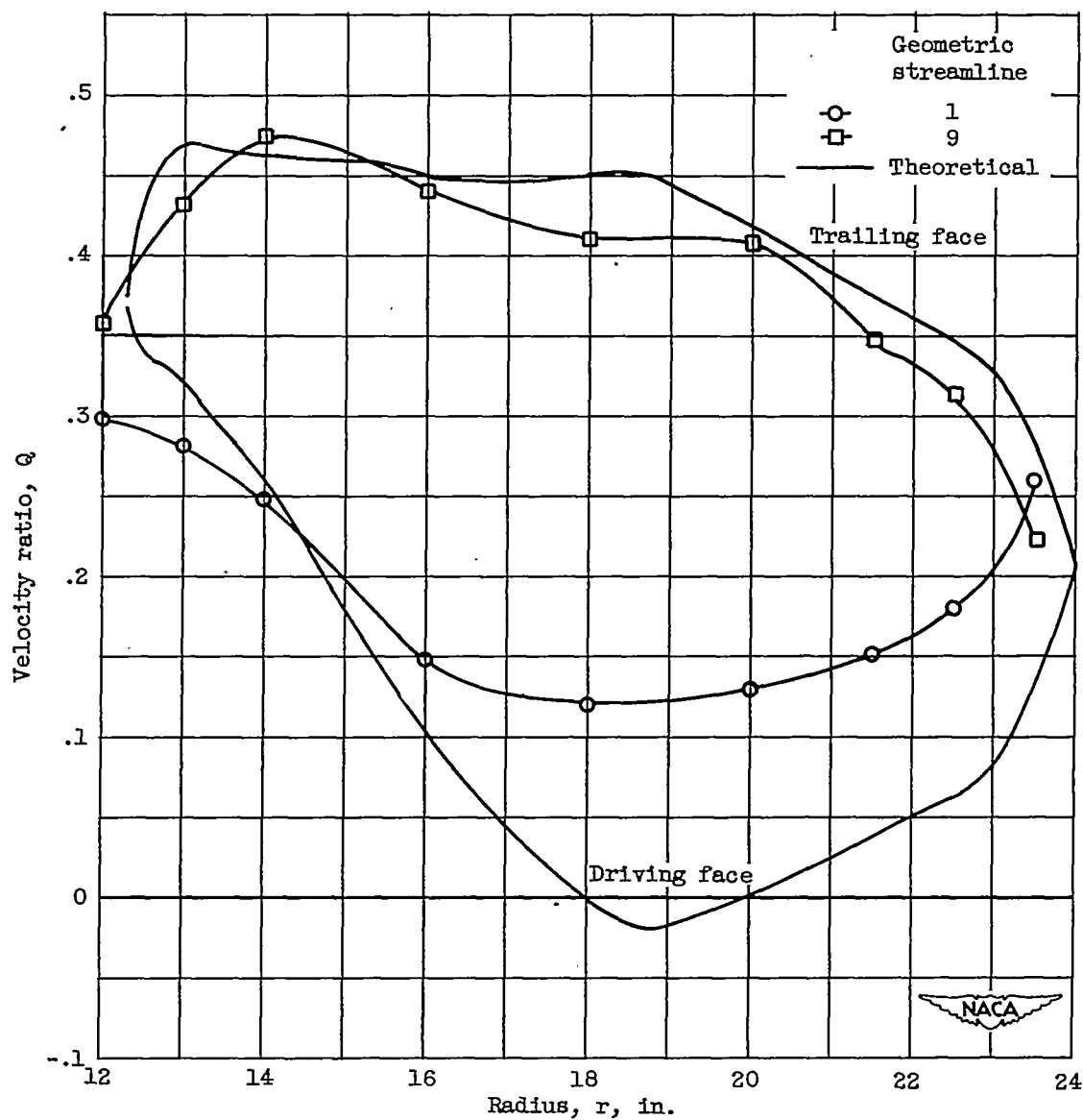
(e) Static-pressure distribution along blade faces.

Figure 5. - Continued. Flow characteristics in impeller rotating passage at corrected weight flow of 26 pounds per second.



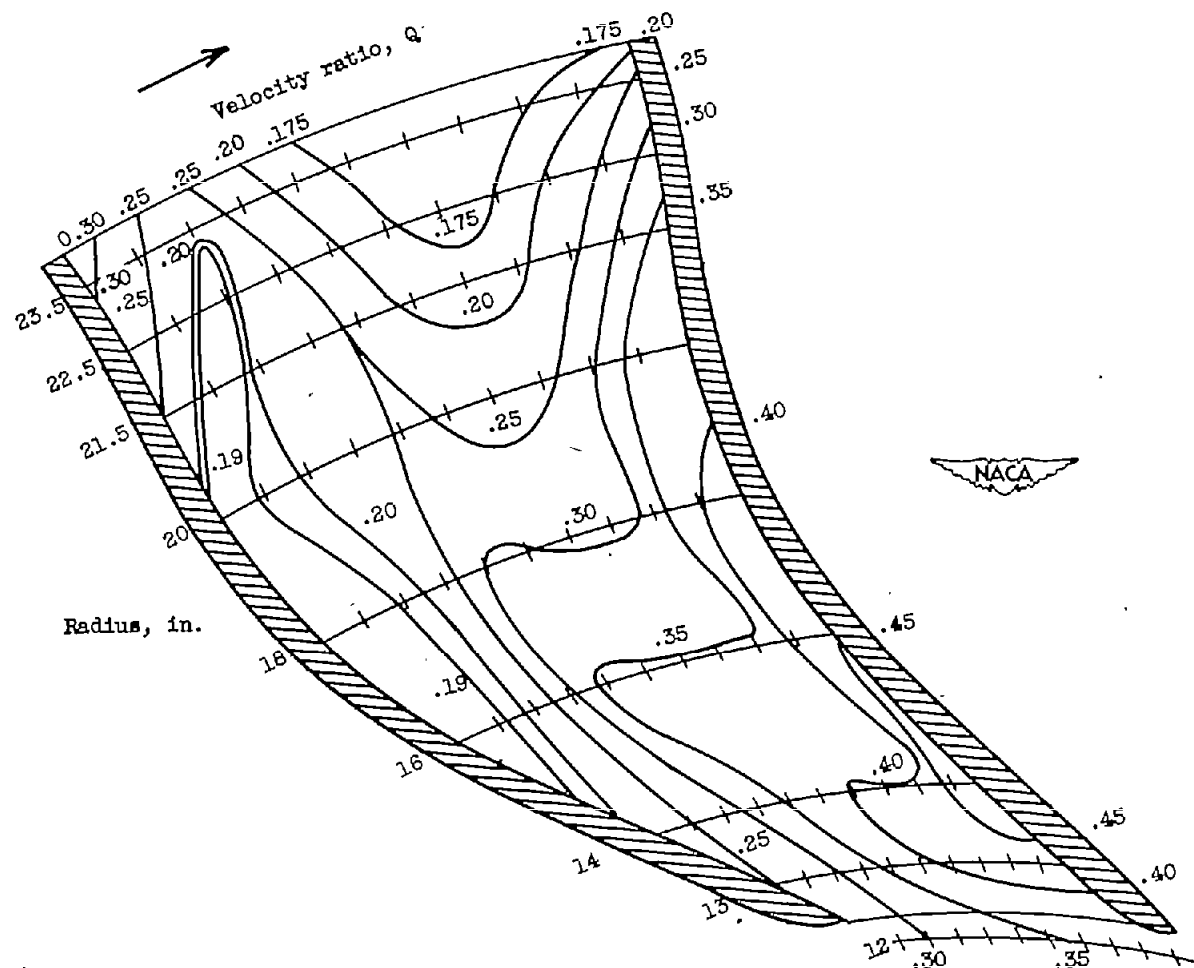
(f) Static-pressure distribution across passage.

Figure 5. - Continued. Flow characteristics in impeller rotating passage at corrected weight flow of 26 pounds per second.



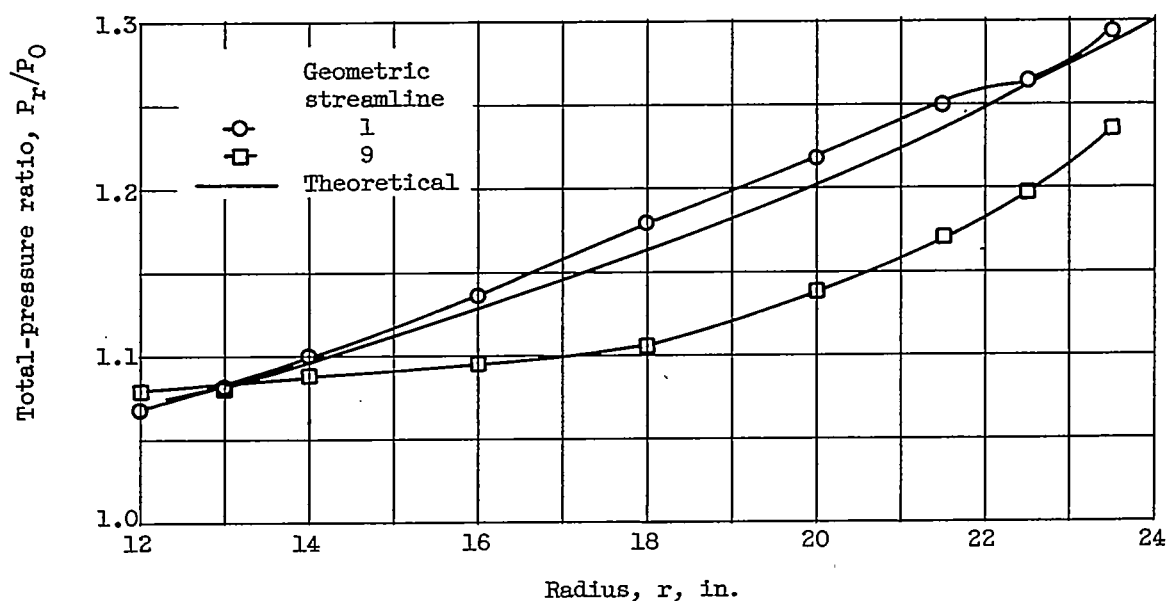
(g) Velocity distribution along blade faces.

Figure 5. - Continued. Flow characteristics in impeller rotating passage at corrected weight flow of 26 pounds per second.

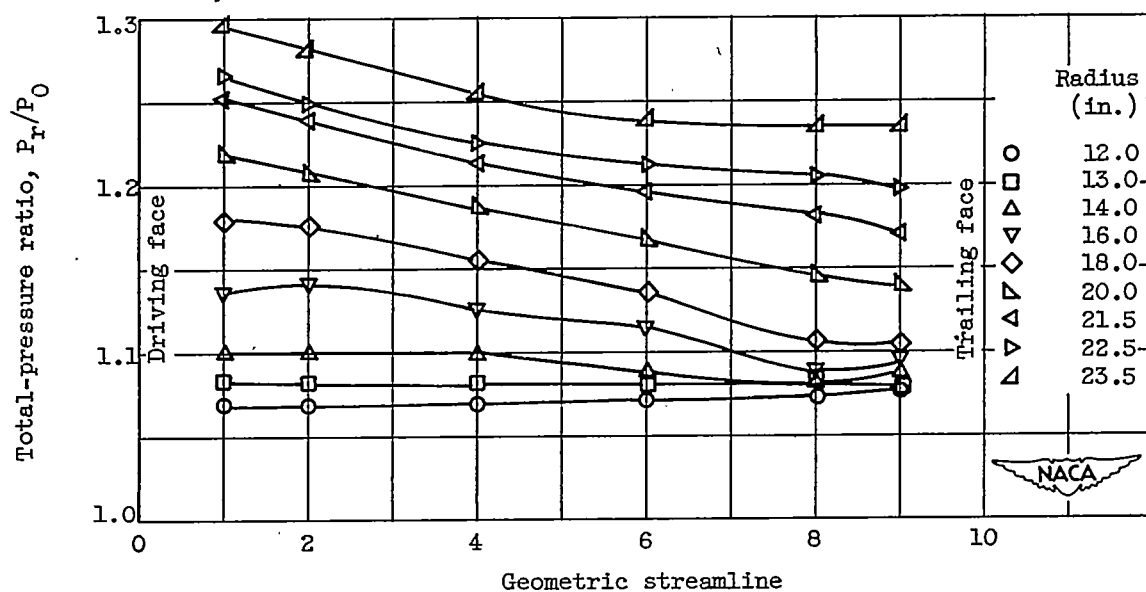


(h) Velocity distribution throughout passage.

Figure 5. - Concluded. Flow characteristics in impeller rotating passage at corrected weight flow of 26 pounds per second.

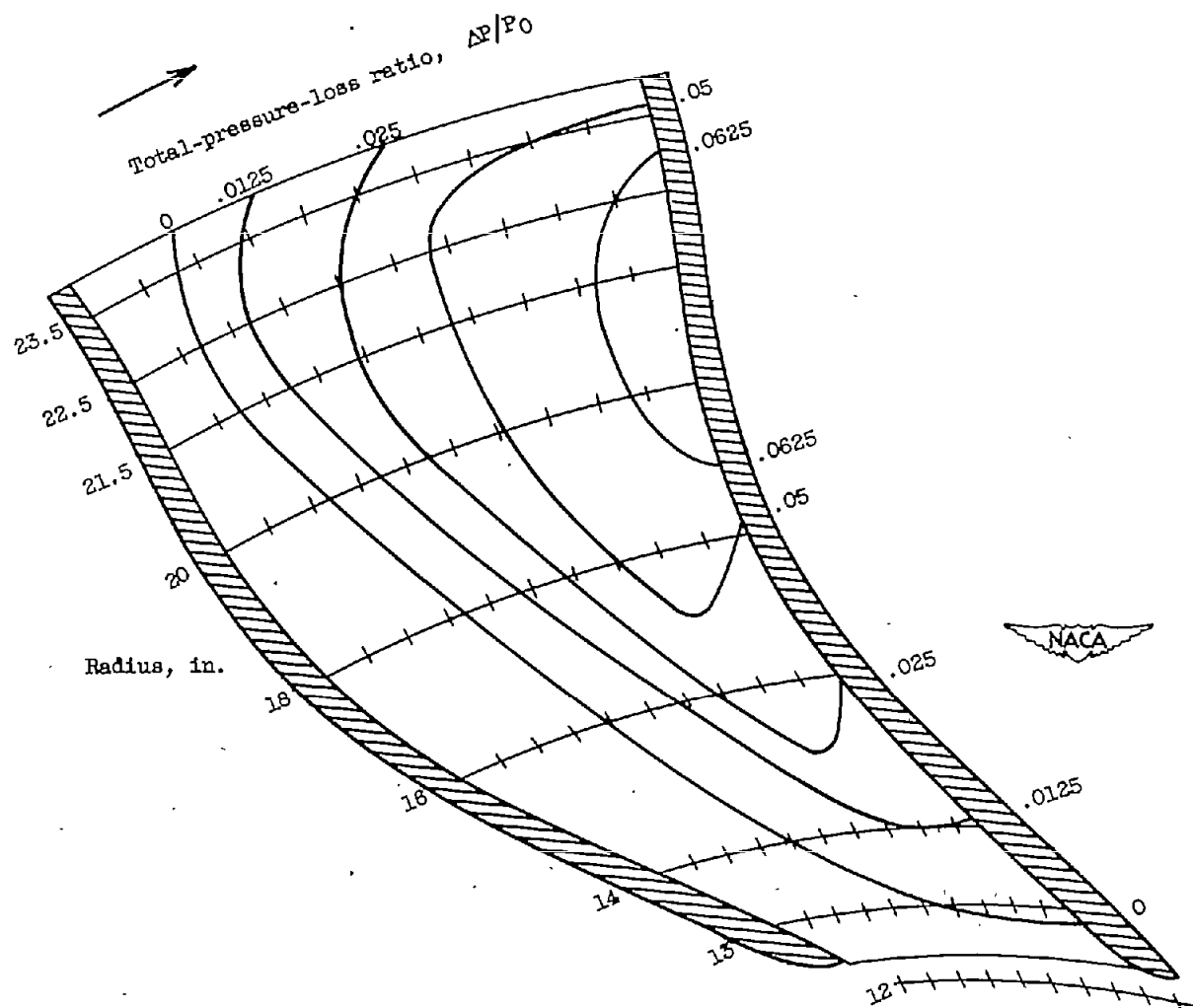


(a) Total-pressure distribution along blade faces.



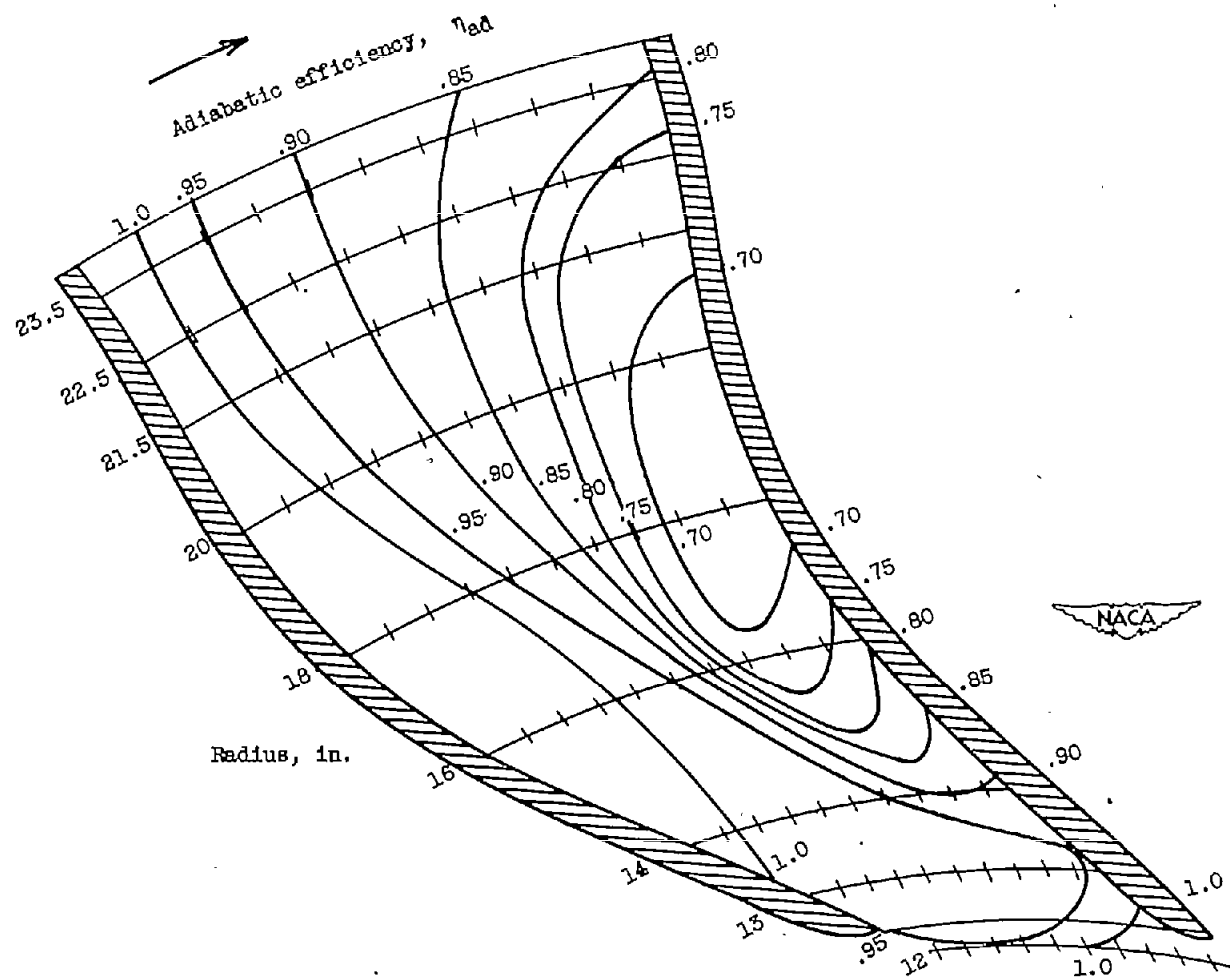
(b) Total-pressure distribution across passage.

Figure 6. - Flow characteristics in impeller rotating passage at corrected weight flow of 14 pounds per second.



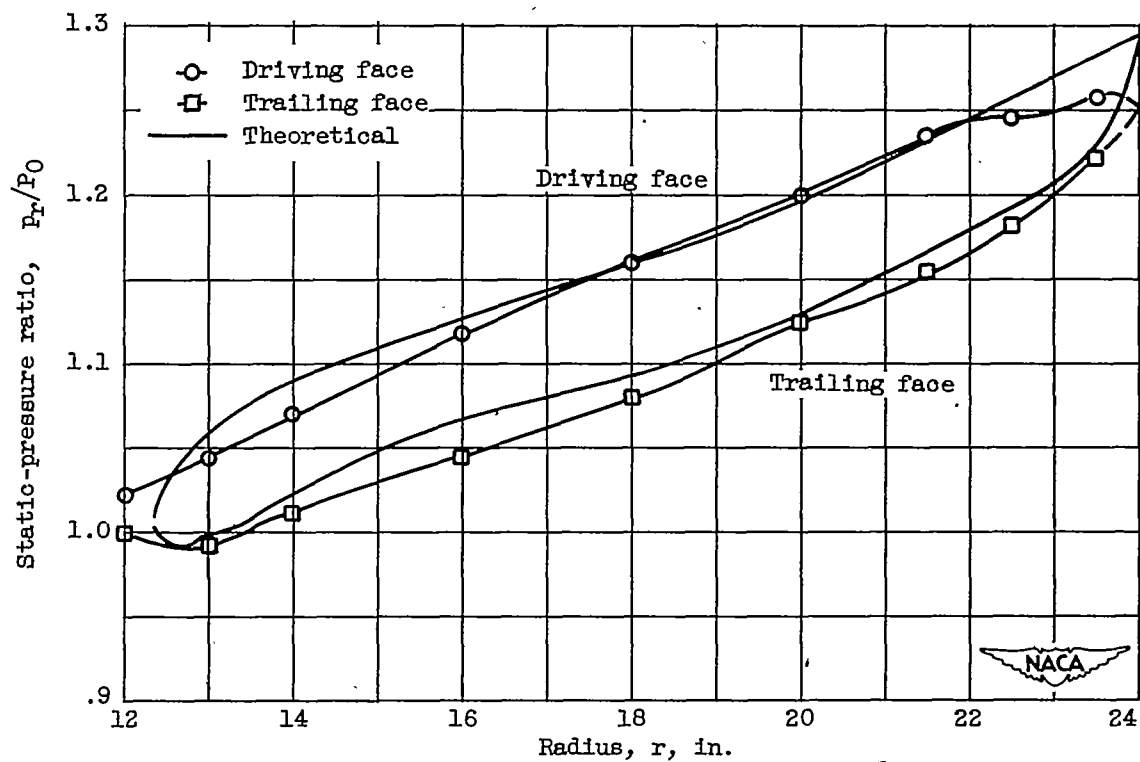
(c) Total-pressure-loss distribution throughout passage.

Figure 8. - Continued. Flow characteristics in impeller rotating passage at corrected weight flow of 14 pounds per second.



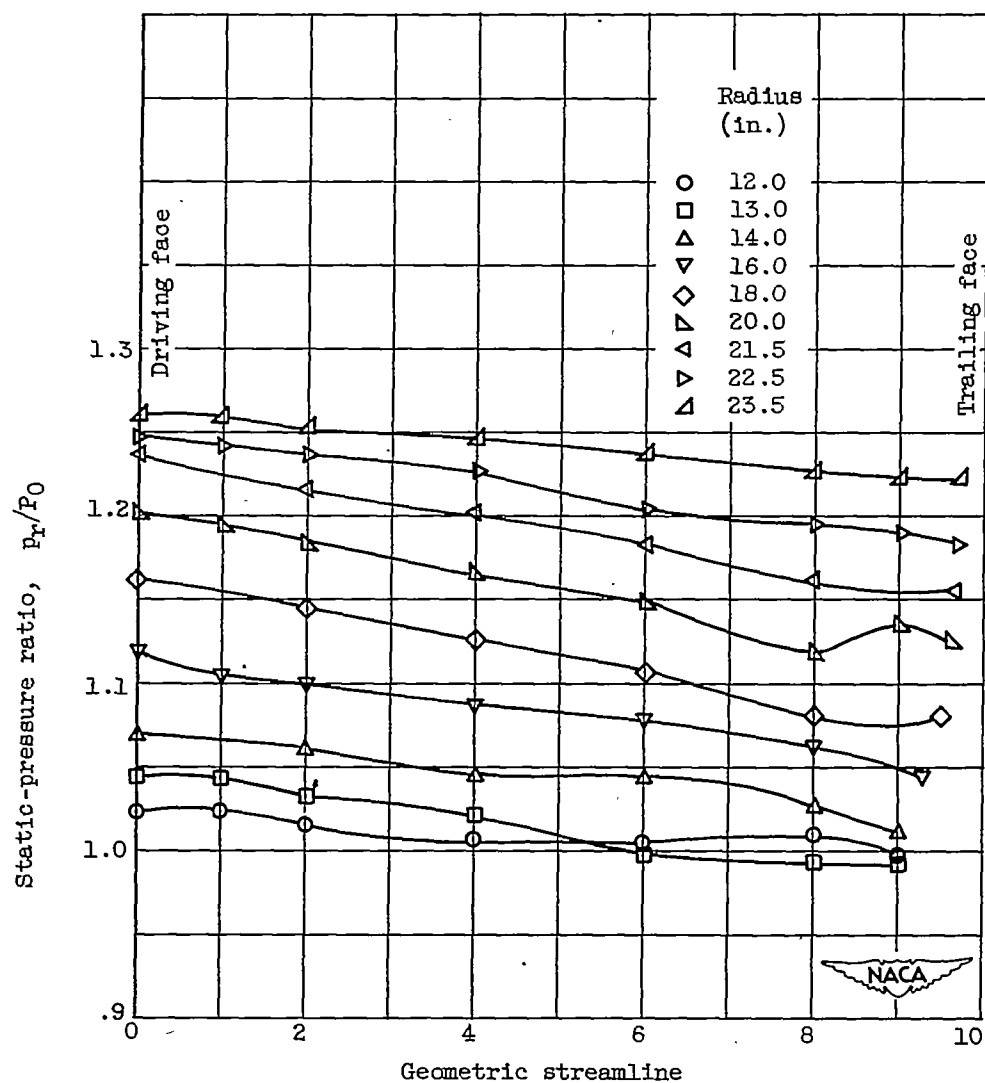
(d) Efficiency distribution throughout passage.

Figure 6. - Continued. Flow characteristics in impeller rotating passage at corrected weight flow of 14 pounds per second.



(e) Static-pressure distribution along blade faces.

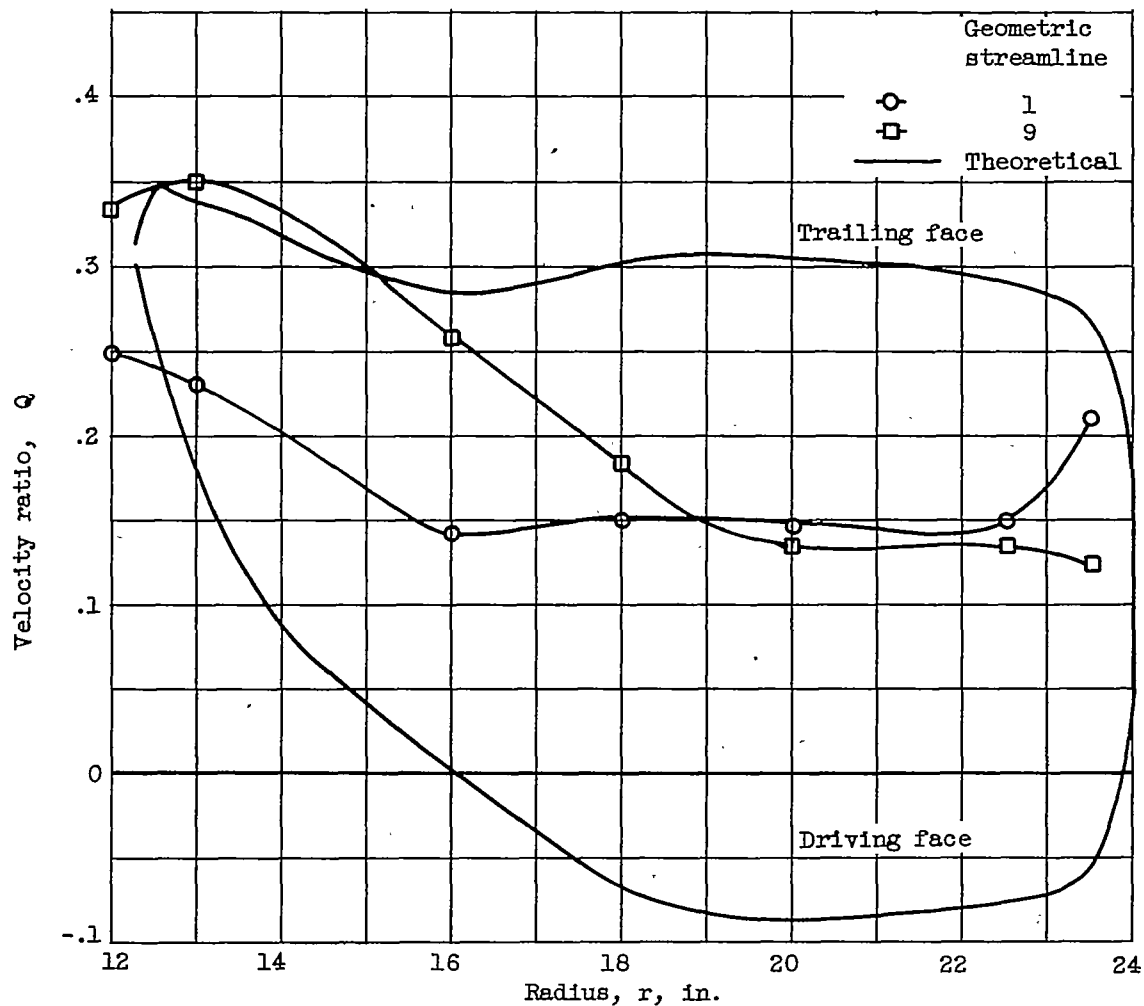
Figure 6. - Continued. Flow characteristics in impeller rotating passage at corrected weight flow of 14 pounds per second.



(f) Static-pressure distribution across passage.

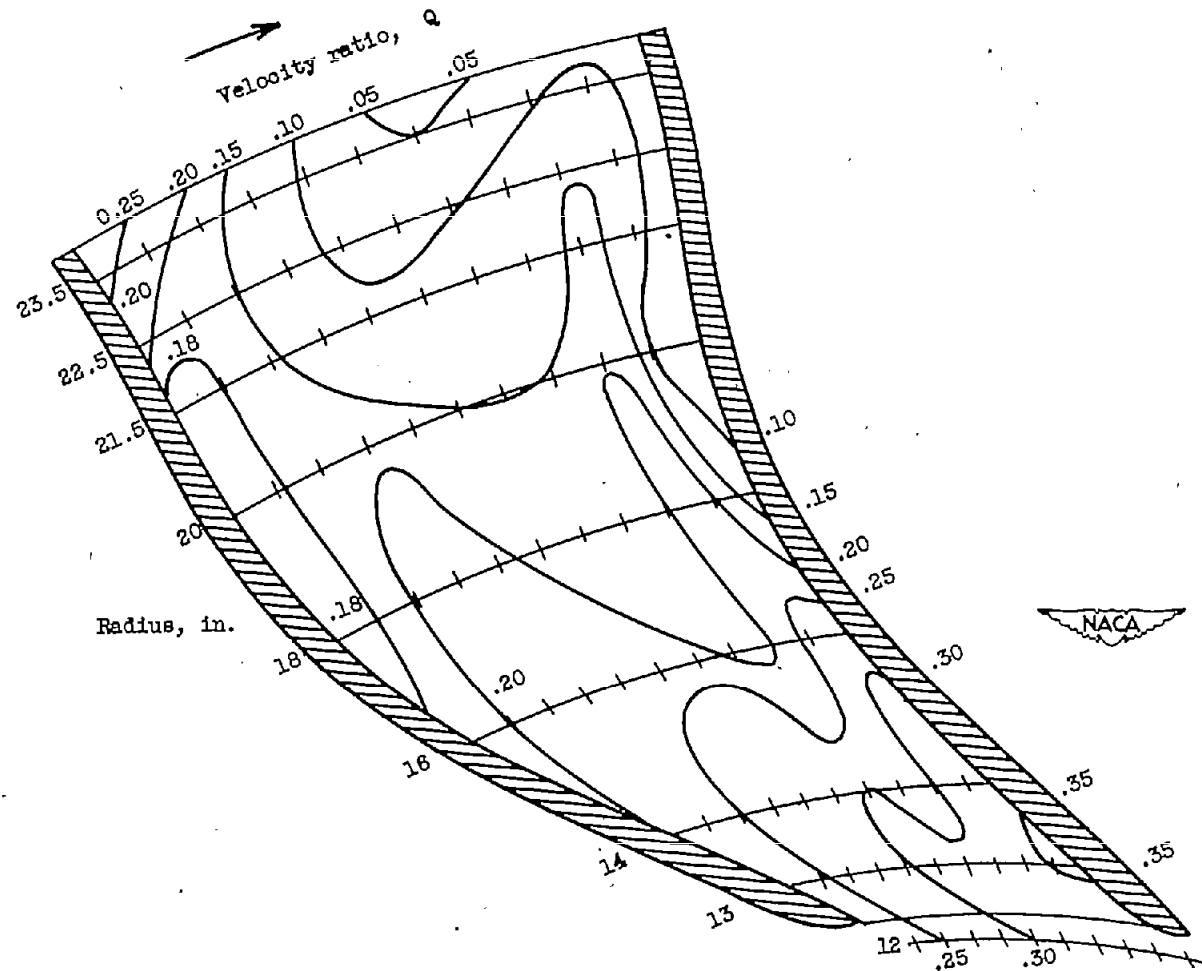
Figure 6. - Continued. Flow characteristics in impeller rotating passage at corrected weight flow of 14 pounds per second.

2376



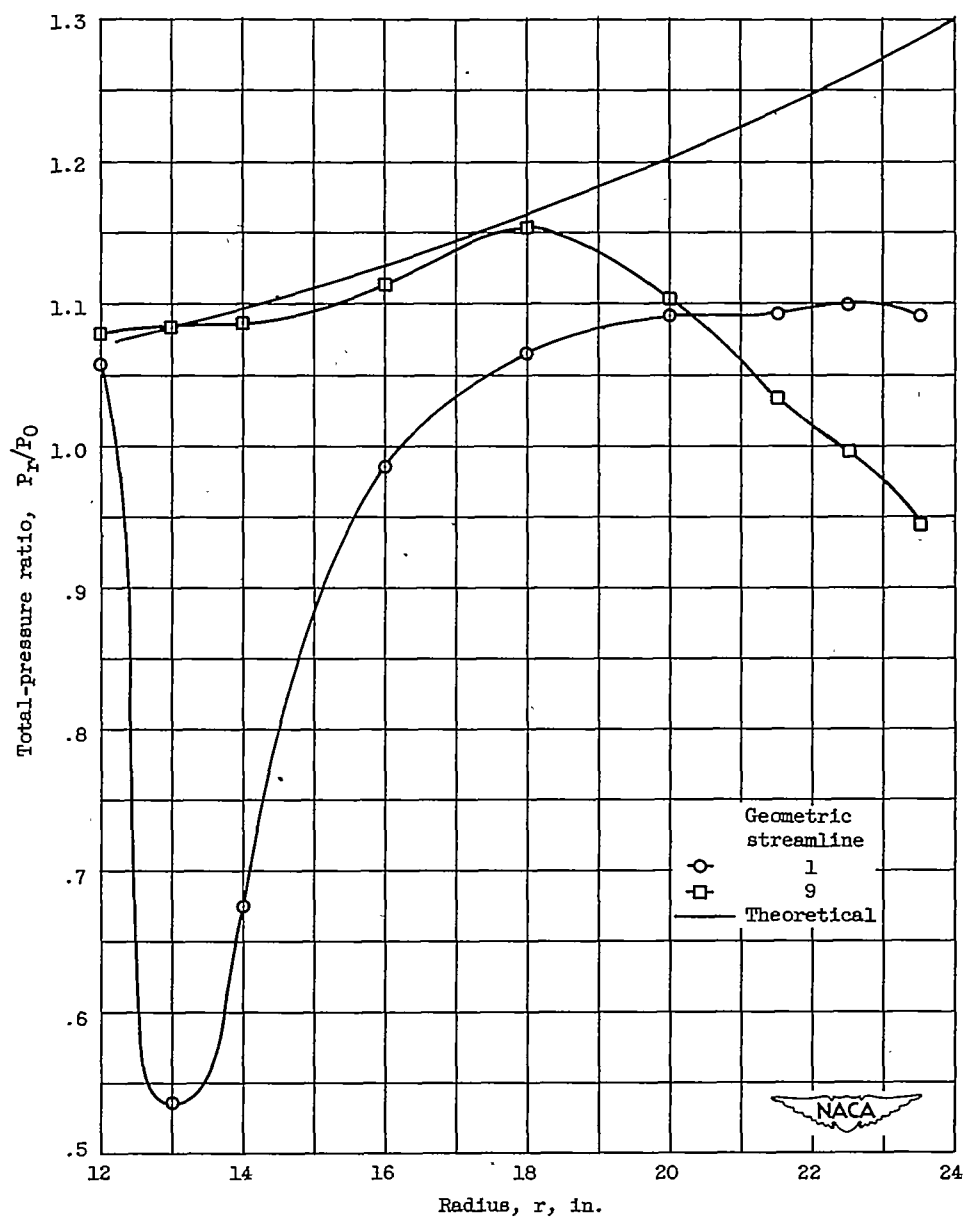
(g) Velocity distribution along blade faces.

Figure 6. - Continued. Flow characteristics in impeller rotating passage at corrected weight flow of 14 pounds per second.



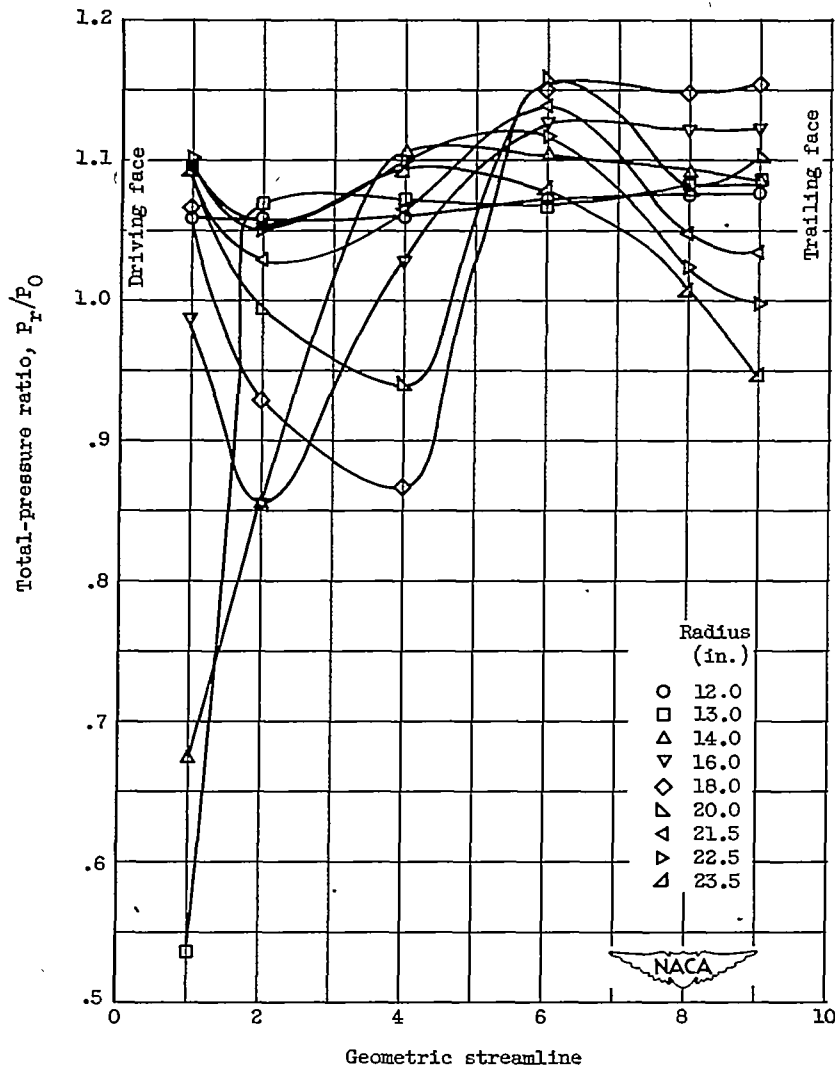
(h) Velocity distribution throughout passage.

Figure 6. - Concluded. Flow characteristics in impeller rotating passage at corrected weight flow of 14 pounds per second.



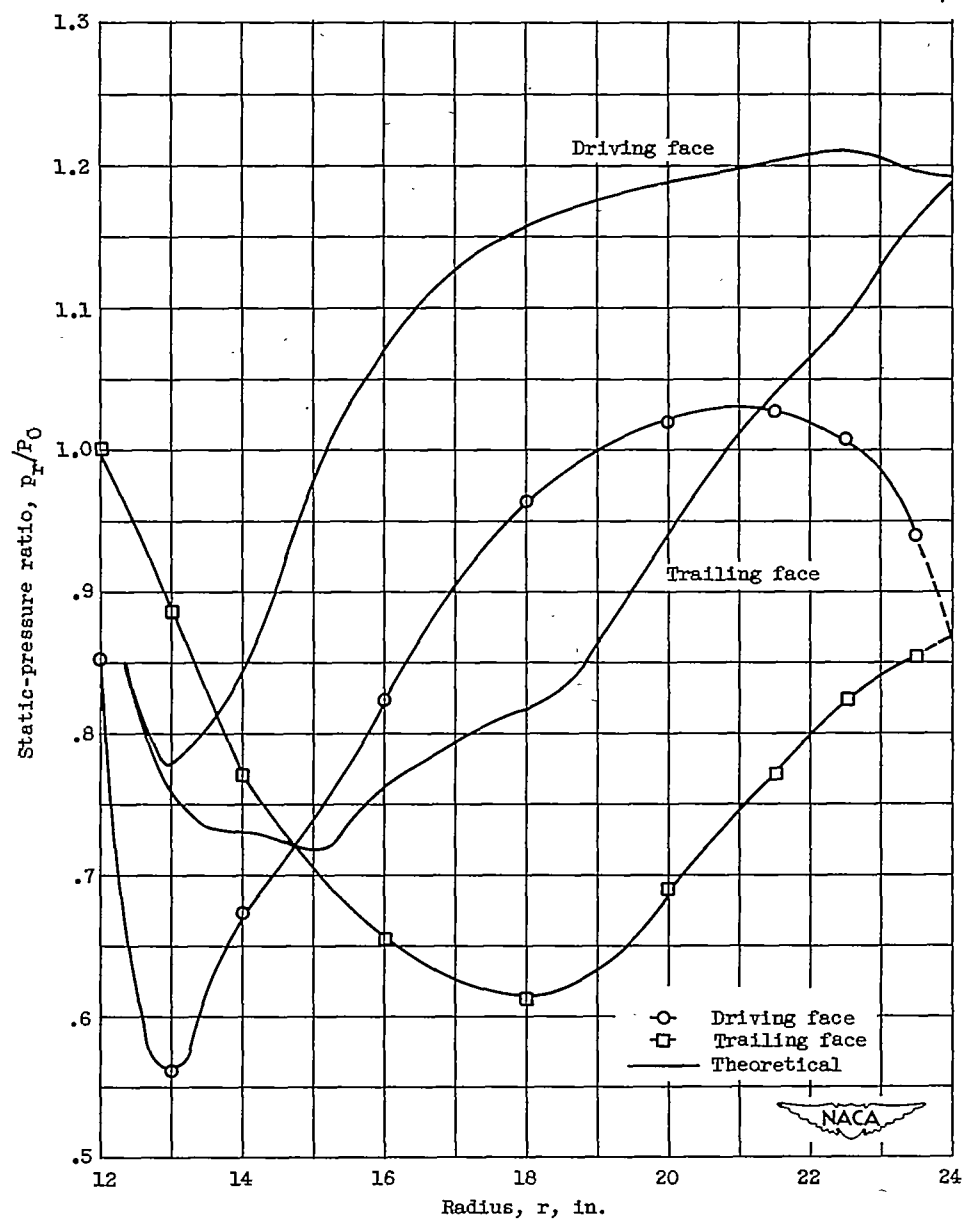
(a) Total-pressure distribution along blade faces.

Figure 7. - Flow characteristics in impeller rotating passage at corrected weight flow of 44 pounds per second.



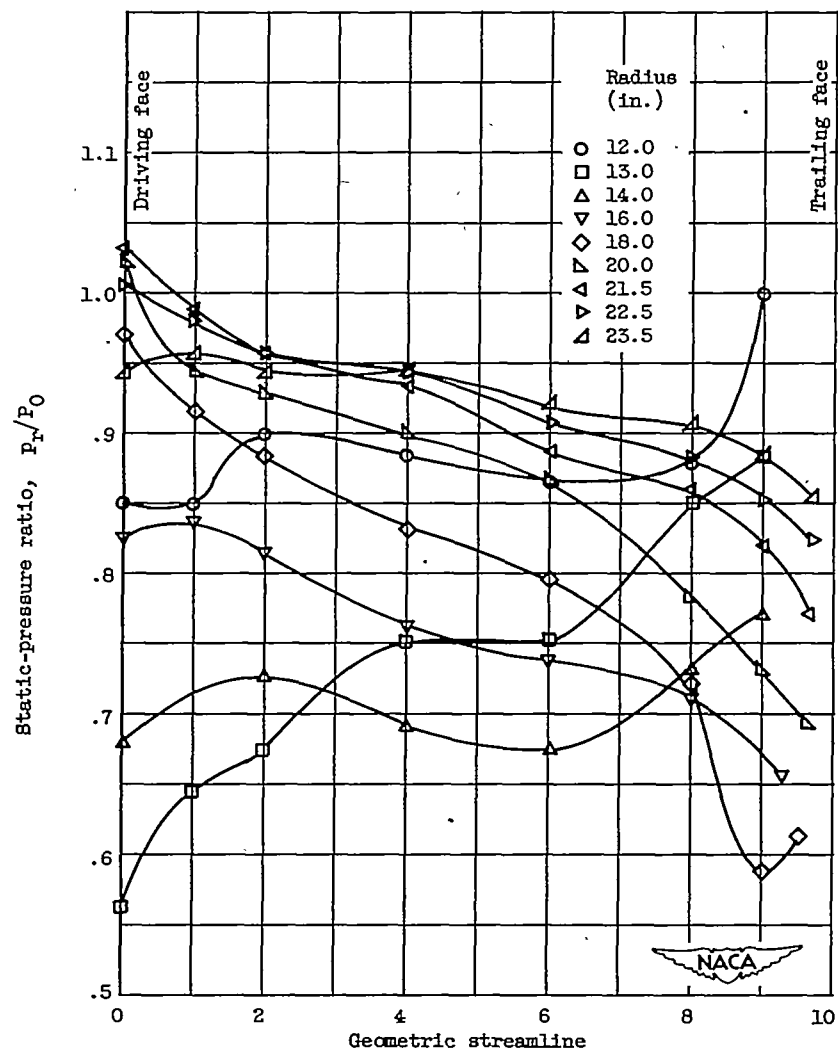
(b) Total-pressure distribution across passage.

Figure 7. - Continued. Flow characteristics in impeller rotating passage at corrected weight flow of 44 pounds per second.



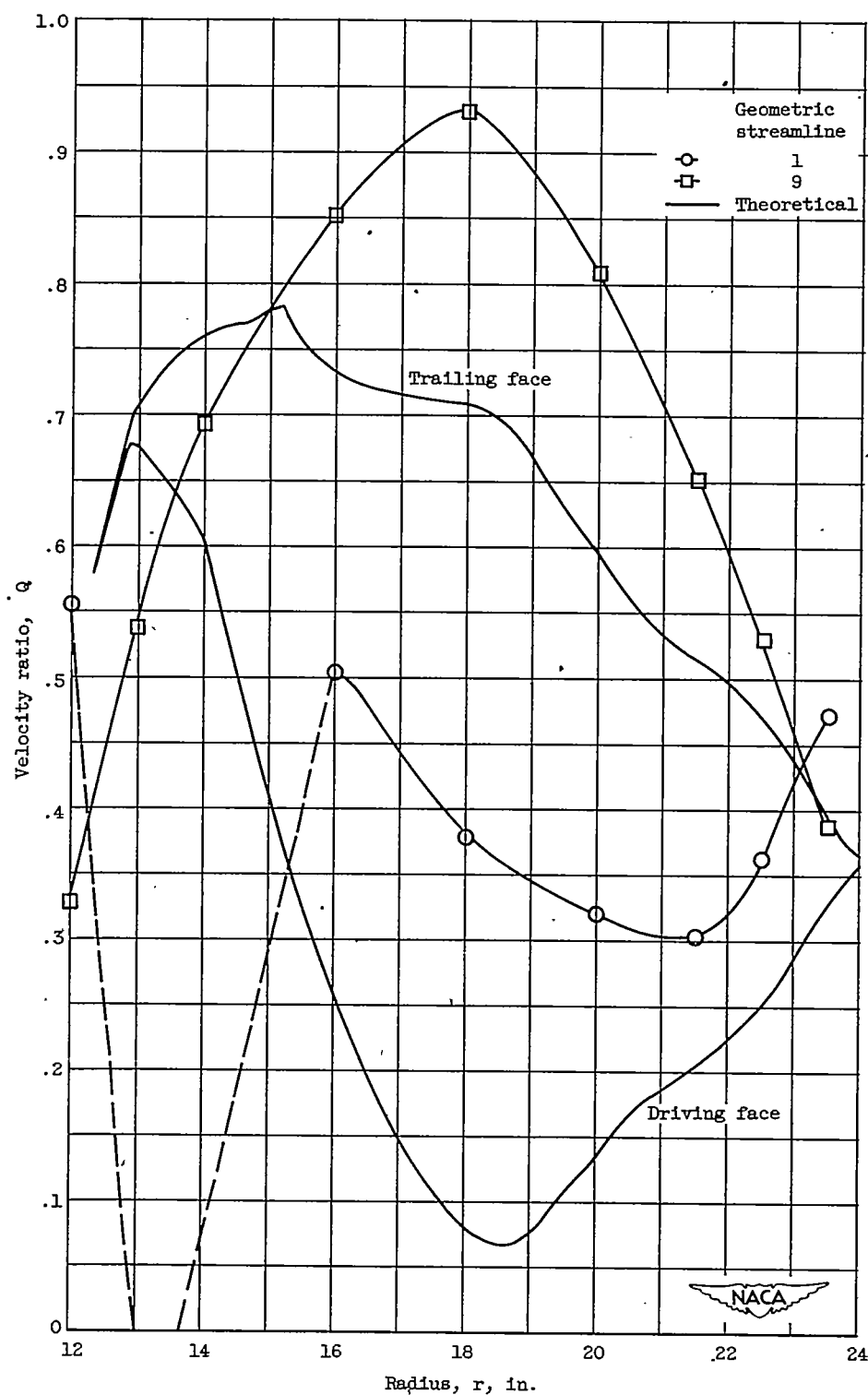
(c) Static-pressure distribution along blade faces.

Figure 7. - Continued. Flow characteristics in impeller rotating passage at corrected weight flow of 44 pounds per second.



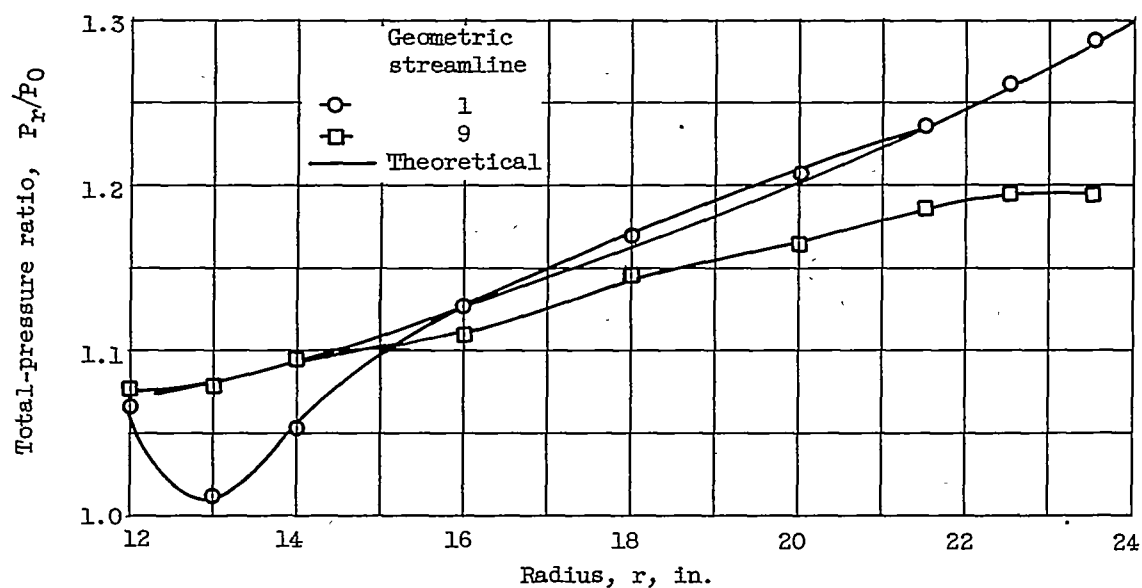
(d) Static-pressure distribution across passage.

Figure 7. - Continued. Flow characteristics in impeller rotating passage at corrected weight flow of 44 pounds per second.

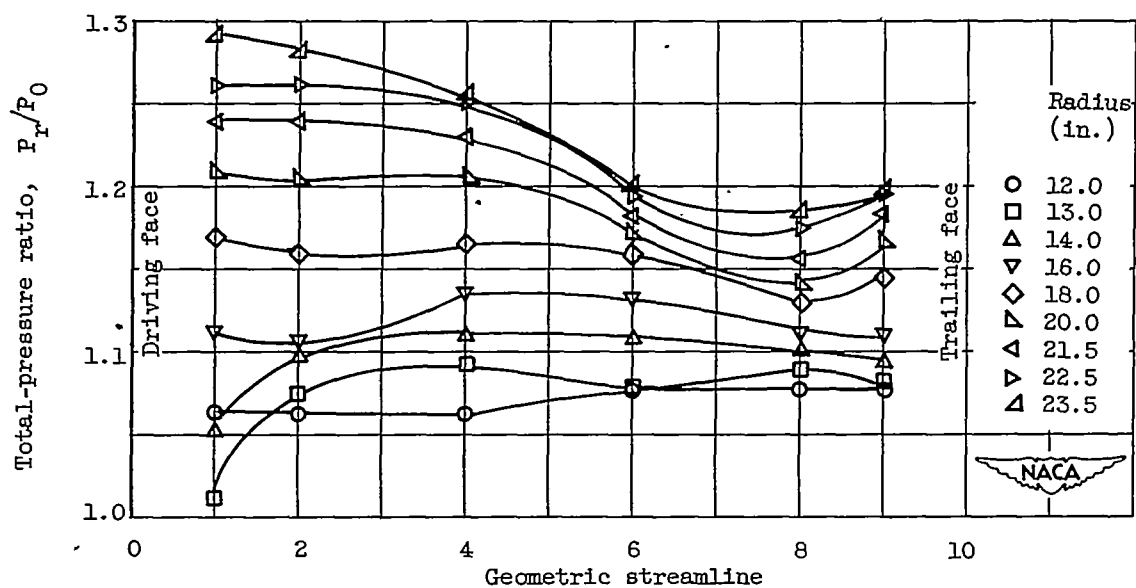


(e) Velocity distribution along blade faces.

Figure 7. - Concluded. Flow characteristics in impeller rotating passage at corrected weight flow of 44 pounds per second.

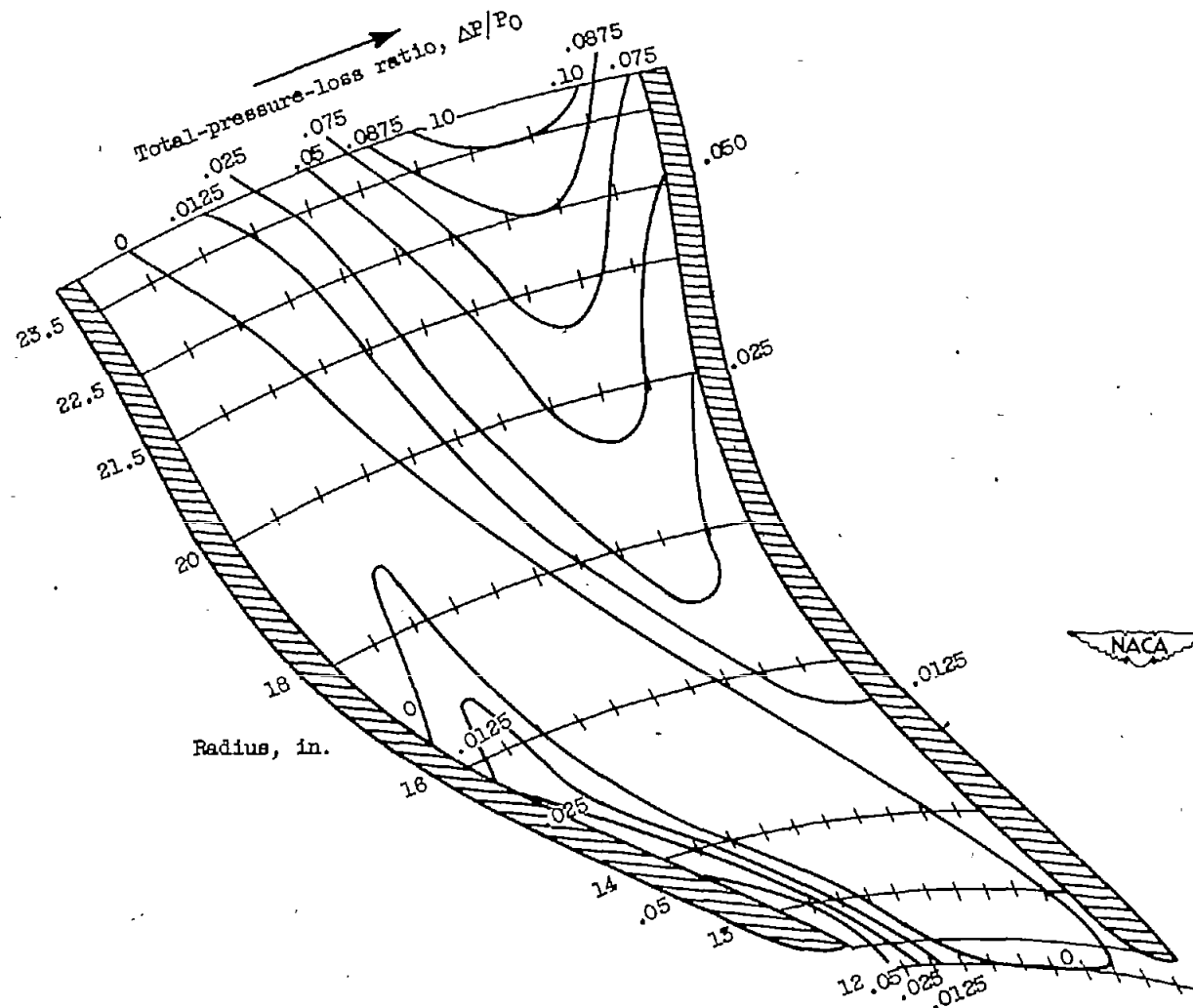


(a) Total-pressure distribution along blade faces.



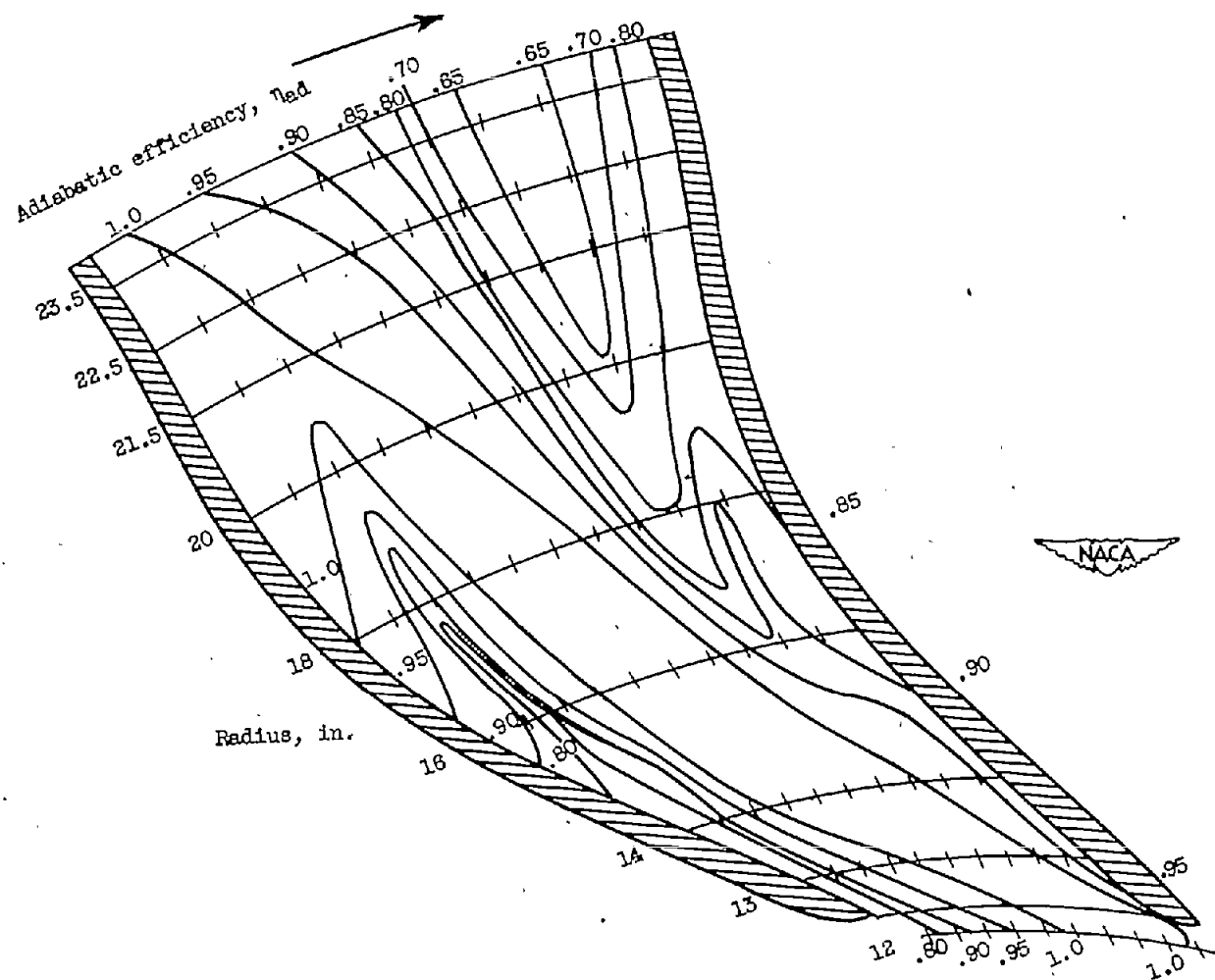
(b) Total-pressure distribution across passage.

Figure 8. - Flow characteristics in impeller rotating passage at corrected weight flow of 32 pounds per second.



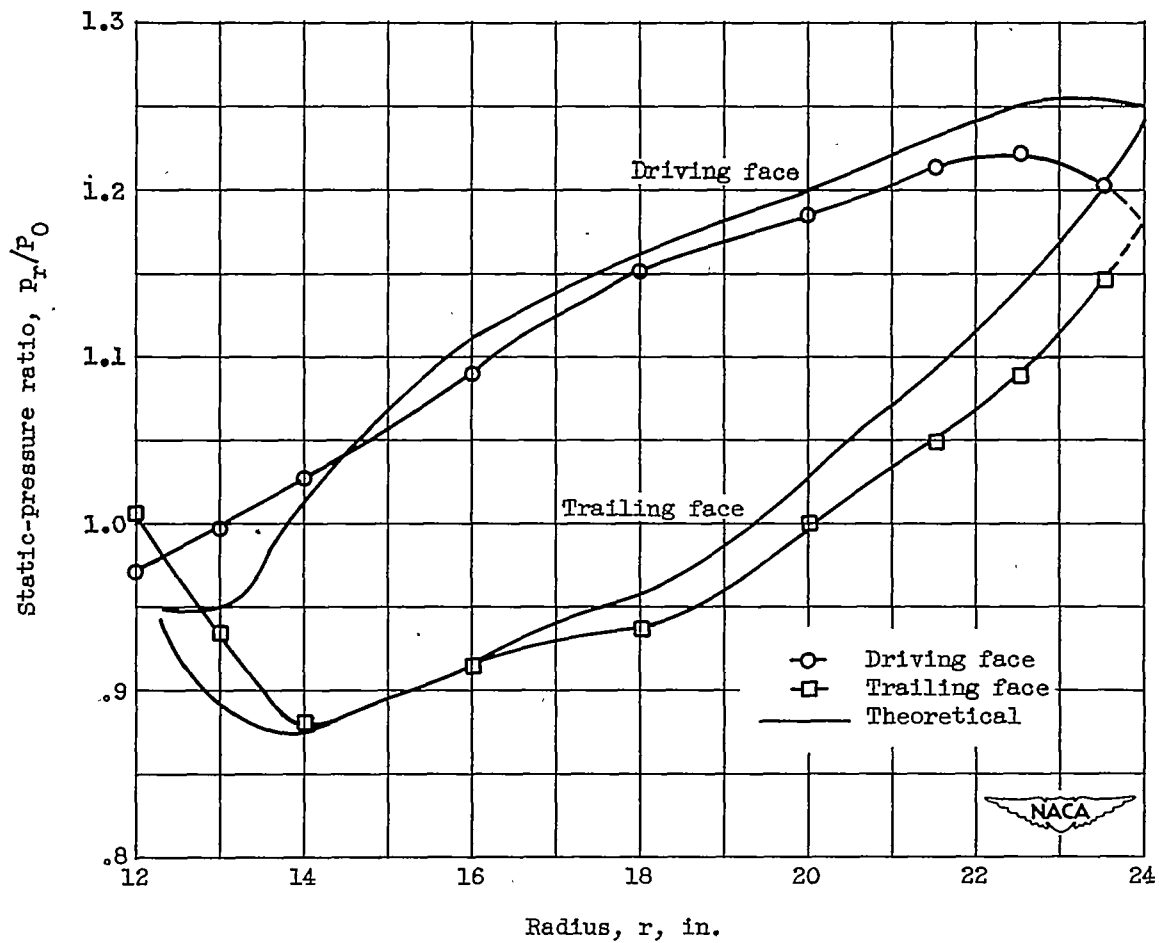
(c) Total-pressure-loss distribution throughout passage.

Figure 8. - Continued. Flow characteristics in impeller rotating passage at corrected weight flow of 32 pounds per second.



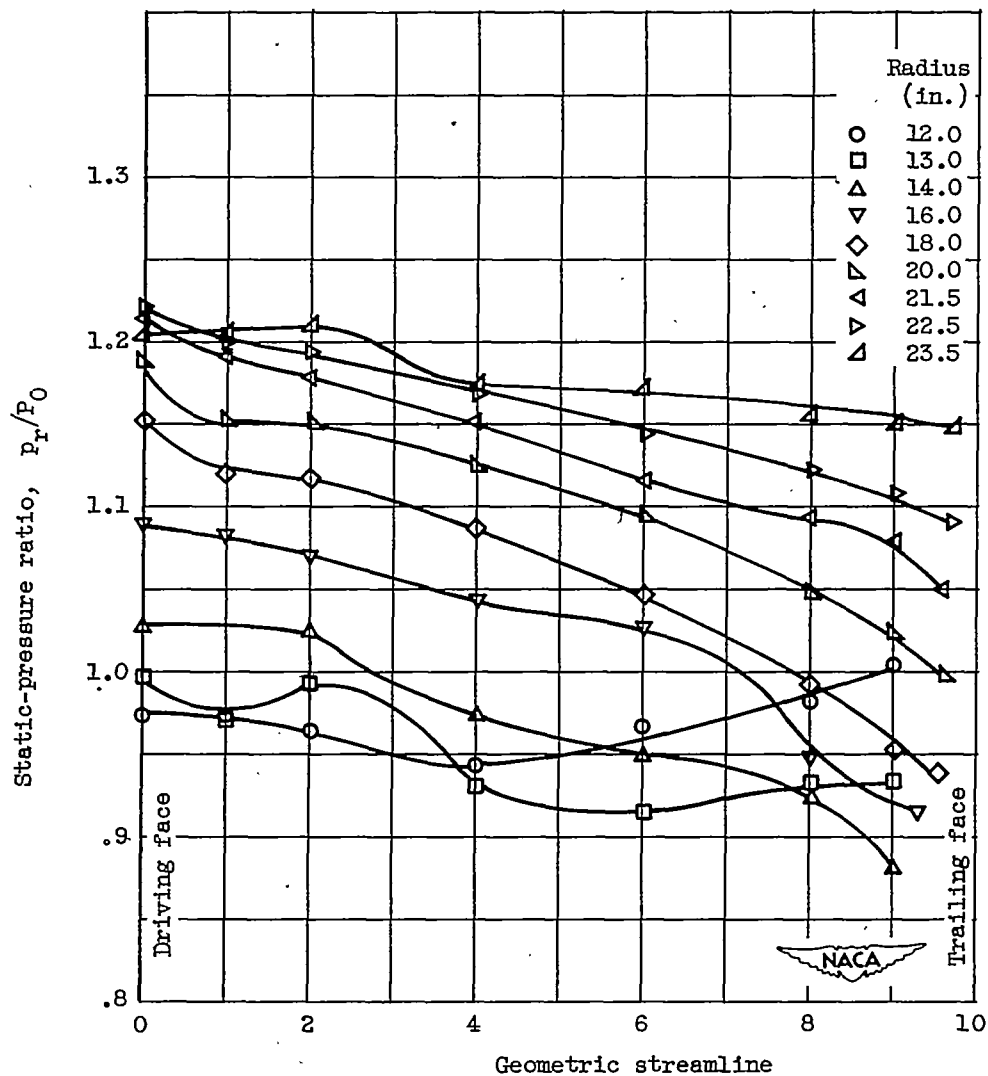
(d) Efficiency distribution throughout passage.

Figure 8. - Continued. Flow characteristics in impeller rotating passage at corrected weight flow of 32 pounds per second.



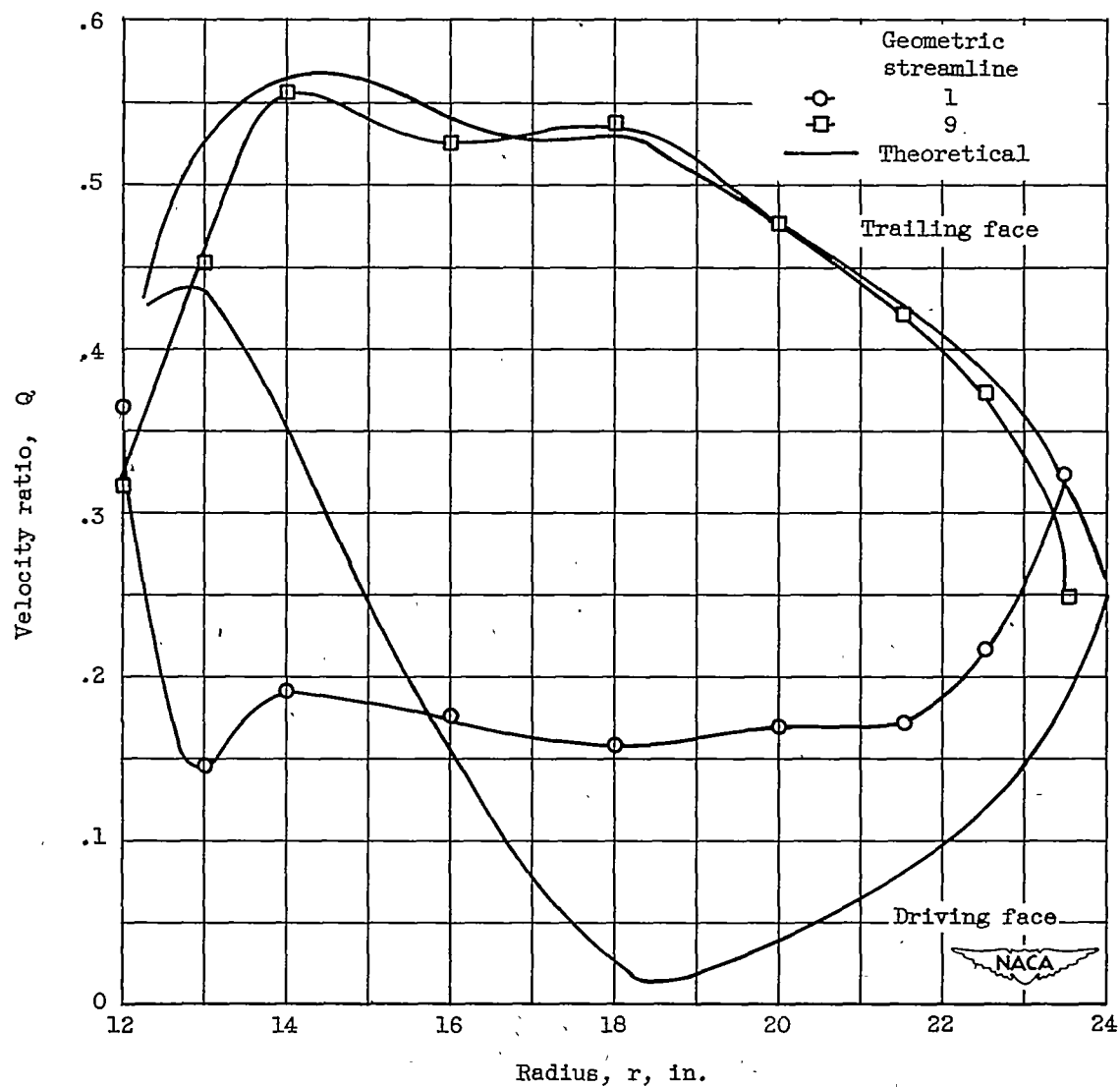
(e) Static-pressure distribution along blade faces.

Figure 8. - Continued. Flow characteristics in impeller rotating passage at corrected weight flow of 32 pounds per second.



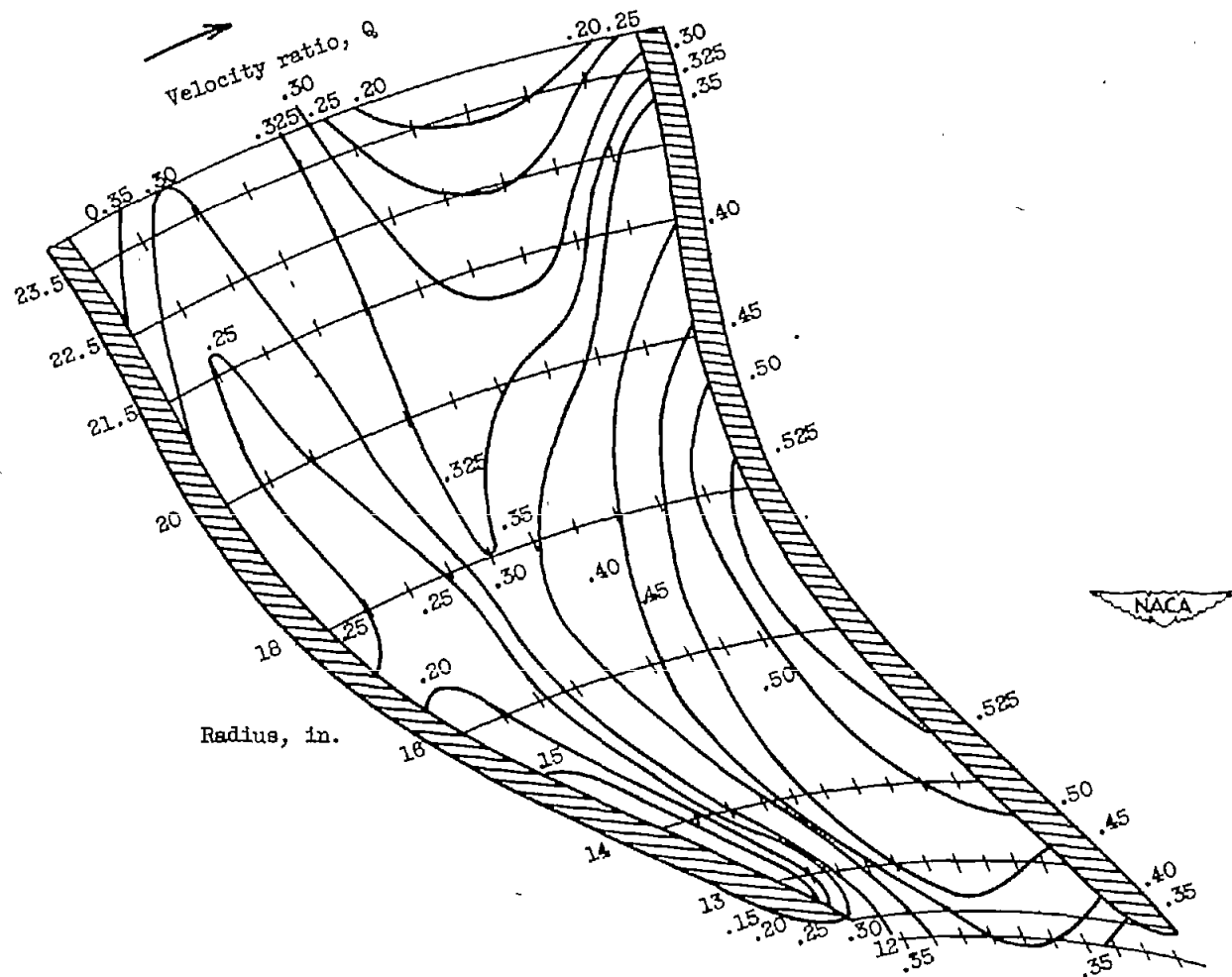
(f) Static-pressure distribution across passage.

Figure 8. - Continued. Flow characteristics in impeller rotating passage at corrected weight flow of 32 pounds per second.



(g) Velocity distribution along blade faces.

Figure 8. - Continued. Flow characteristics in impeller rotating passage at corrected weight flow of 32 pounds per second.



(h) Velocity distribution throughout passage.

Figure 8. - Concluded. Flow characteristics in impeller rotating passage at corrected weight flow of 32 pounds per second.